# INSTRUMENTAL MEASUREMENTS LABORATORY

Dr. Ethem İlhan ŞAHİN
Assist. Prof. Mehriban EMEK
Dr. Jamal Eldin Fadoul Mohammed IBRAHIM

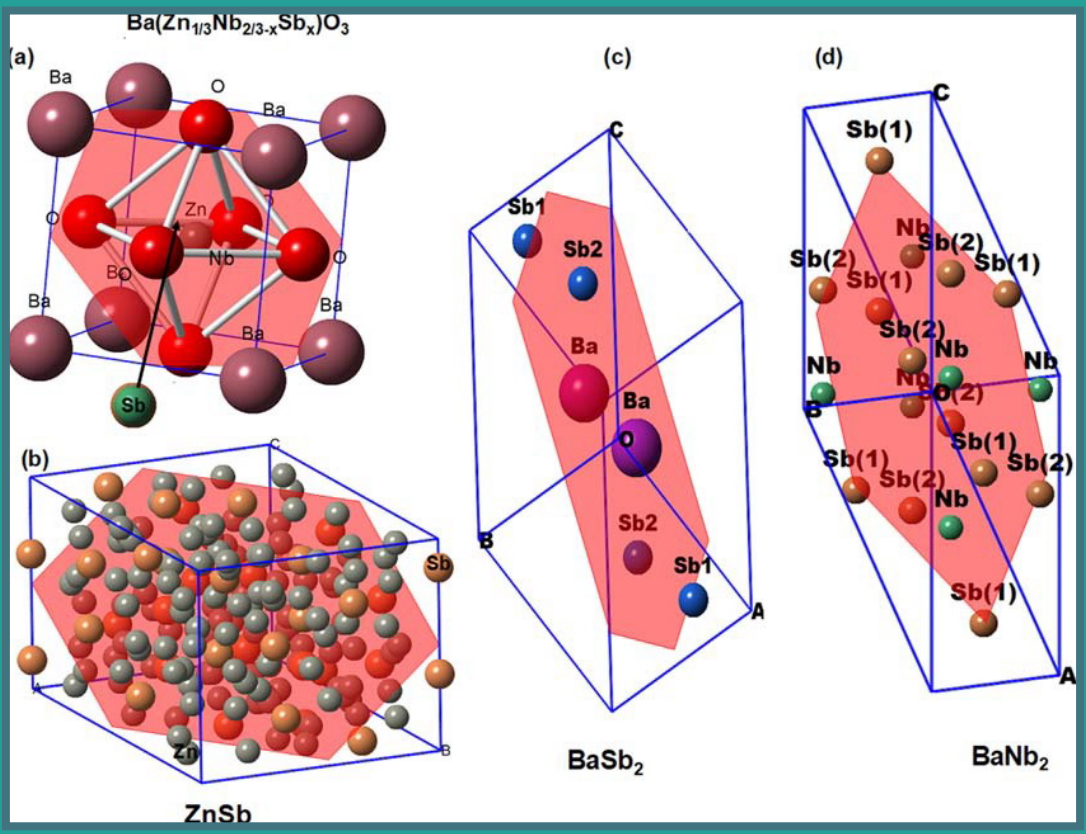


İKSAD
Publishing House

# INSTRUMENTAL MEASUREMENTS LABORATORY

**Dr. Ethem İlhan Şahin[1]**

**Assistant Professor Mehriban EMEK[2]**

**Dr. Jamal Eldin Fadoul Mohammed IBRAHIM[3]**

İKSAD Publishing House

[1] Dr., Adana Alparslan Türkeş Science and Technology University, Advanced Technology Research and Application Center, Adana, 01250, Türkiye. shnethem@gmail.com, ORCID ID :0000-0001-7859-9066

[2] Assistant Professor, Adıyaman University, Gölbaşı Vocational School, Department of Computer Technologies, Gölbaşı Adıyaman, Türkiye. emekmehriban@gmail.com, ORCID ID: 0000-0001-7322-9808

[3]Dr., University of Miskolc, Doctoral School of Material Science and Technology, Institute of Ceramic and Polymer Engineering, Faculty of Material Science and Engineering, Miskolc, Hungary), Macaristan. jamalfadoul@gmail.com, ORCID ID: 0000-0003-2479-5955

(The Licence Number of Publicator: 2014/31220)
TURKEY TR: +90 342 606 06 75
USA: +1 631 685 0 853
E mail: iksadyayinevi@gmail.com
www.iksadyayinevi.com
It is responsibility of the author to abide by the publishing ethics rules.
Iksad Publications – 2023©
**ISBN: 978-625-367-083-2**
Cover Design: İbrahim KAYA
May / 2023
Ankara / Turkey
Size = 16 x 24 cm

# PREFACE

Dear researchers and readers, this book has been formatted by giving basic examples for instrumented measurement laboratories, as well as giving summarized information on instrumental measurements required in materials science and many other fields.

By including both theoretical information and practical guidance, the book serves as a valuable resource for both beginners and experienced professionals. It not only introduces the fundamental measurement techniques but also provides insights into the overall measurement process, ensuring that readers have a comprehensive understanding of how measurements are performed and how the results are evaluated.

In this first edition, some basic technological devices are included with sample measurements, and in the next edition, information about other devices will be included with examples. We believe that our book will bring a different perspective to researchers, many students and laboratory workers and will open new horizons in the realm of measurement techniques.

We also hope that it will be tested and evaluated in applied fields, ultimately serving as a valuable reference in scientific research.

This work is dedicated to the memory of Salim Şahin and Emsal Şahin, as well as Prof. Dr. Ayhan Mergen.

Thank you to those who contributed to the publication of the book. We also wish God's mercy on those who lost their lives in the earthquake in our country on February 6, 2023.

Dr. E. I. SAHIN

Asst. Prof. M. EMEK

Dr. J. E. F. M. IBRAHIM

# CONTENTS

# 1. INTRODUCTION

Recent years have witnessed remarkable advancements in superior materials, accompanied by significant growth in the communication, production, and health industries. As a result, there has been an enormous increase in material demand across various sectors.

Characterizing materials in detail is crucial for understanding their properties and identifying their unique characteristics.

New technologies and device instrumentation are being employed to enhance the characterization of various materials, including doped, undoped, composite, and polymer-based materials. This enables better control and understanding of their properties and outcomes. Innovative solution approaches are also being utilized to achieve optimal results in material characterization.

To characterize materials, the most common instruments are XRD, SEM, SEM coating device, XPS, FTIR, TG-DTA, Two-port vector network analyzer (VNA), Network analyzer (NA), IRMS, inverted microscopes, MP imaging system device, dielectric measuring device, VSM, GC/MS, and Ion chromatography (IC). These tools are utilized depending on the method and kind of the material.

Material characterization has many different types, including structural, physical, mechanical, chemical, optical, morphological, absorptive, reflective, electrical and magnetic.

These technical measuring tools may identify several characterization factors, including chemical composition, internal structure, surface area, solubility, porosity, crystalline structure, and surface charge.

The book provides details and examples of measurement results from the most popular measuring tools, which are typically used to identify materials and highlight their distinctive characteristics.

As is common knowledge, characterization of the material is done using cutting-edge tools in order to fully comprehend the different materials before production; it enables researchers to assess the behavior of materials in diverse environmental conditions and to ascertain their various structural, electrical, chemical and physical properties.

The book comprises 14 chapters, wherein the measurement of samples commences after presenting concise definitions for device characterization.

With the measurements, the material definition and characteristics were examined in detail.

As the book progresses to its final sections, the test results are presented by exemplifying measurements conducted on various devices.

The results of electromagnetic reflection loss and shielding efficacy of materials with VNA and NA devices over a broad frequency range, which are thought to be crucial for many sectors, are also presented in the 12th chapter.

Measurement methods are also presented, which are going to be crucial for future studies**.**

## 2. INVERTED MICROSCOPE (ZEISS AXIO VERT. A1)

### 2.1. General Information

The microscope is specifically designed for conducting studies on cell and tissue culture, as well as microinjection units. It features an objective lens positioned at the bottom of the microscope, which incorporates phase contrast capabilities. This configuration enables enhanced visualization and analysis of samples (Helmers et al., 2022).

You can get significant insights with the little, inverted microscope known as Axio Vert.A1 (Figure 1).

You may study samples using a variety of traditional and cutting-edge contrast techniques.

You may quickly switch between reflected light with darkfield, brightfield, C-DIC, DIC, fluorescence, and polarization contrast.

Your construction can be efficiently quantified, and the qualities and characteristics of your materials can be evaluated.

It is designed for genetic research. With its integrated camera and computer program, it allows the cells to be viewed and photographed on the computer screen. In the microscope, the objective lenses are located at the bottom of the table.

Focus adjustment is provided by the vertical movement of the part where the lenses are attached; the table remains in a fixed position. Focusing is done with the interlocking fine and coarse adjustment knobs on either side of the microscope. It is in a more advantageous position than plain light microscopes for imaging organisms in a large container, such as living cells or tissue culture, in natural conditions (Helmers et al., 2022).

It was developed and designed as an ideal solution for fast and reliable routine work in both brightfield and phase contrast methods. The glass table surface provides easy viewing and tracking of the objective turret.


**Figure 1.** Inverted Microscope- Zeiss Axio Vert. A1 (www.zeiss.com/axiovert)

It has been designed in accordance with the work of versatile advanced laboratories.

Thanks to its versatile modular feature, it can be used for bright field, dark field and phase contrast techniques.

The illumination source illuminates the sample more uniformly and homogeneously, resulting in lower consumption and longer life.

## 2.2. A General Sample Measurement

To examine the microstructure of the etched surfaces in the sample of the aluminum alloy below (Figure 2), the contrast method of the reflected light brilliant field was applied.

It is possible to determine the sizes, phases, and structural elements of grains by observing hues and pigments and spotting grain borders.

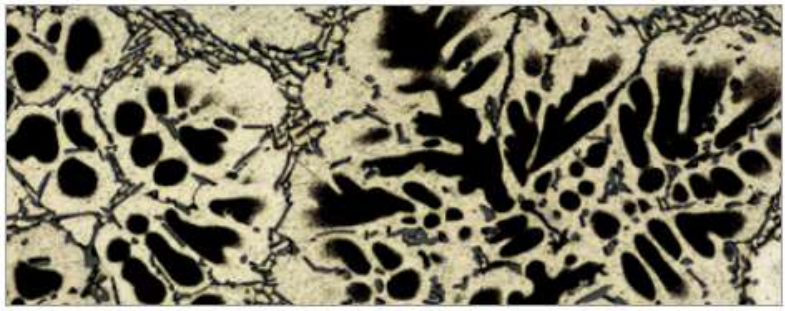

**Figure 2.** Aluminium Alloy, 100x, Brightfield (Inverted Microscope- Zeiss Axio Vert. A1) (www.zeiss.com/axiovert, www.zeiss.com/axiovert-mat)

Impurities and structural elements, including cast iron's graphite, can be detected prior to etching.

The use of polarization contrast is necessary to examine the structure of anisotropic materials. The individual crystal lattice grains for pure magnesium below revealed their own hue when seen under Polarized light (Figure 3) (www.zeiss.com/axiovert-mat).

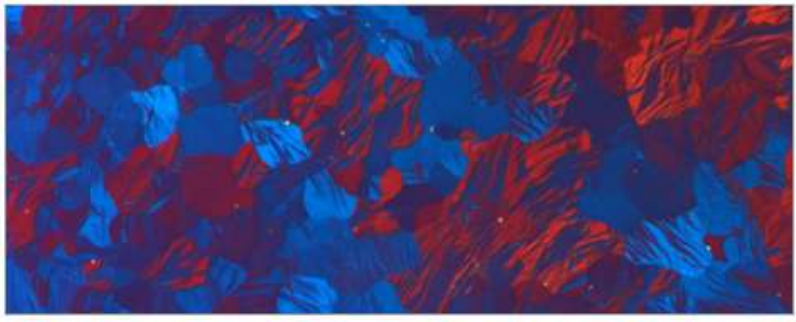

**Figure 3.** Pure Magnesium, 100x, Polarization (Inverted Microscope- Zeiss Axio Vert. A1) ( www.zeiss.com/axiovert, www.zeiss.com/axiovert-mat)

Specifically, when the corrosion characteristics of the CuSnSi alloy in various environments are studied using an optical microscope in our study that follows (Şahin and Cantürk, 2022);

Corrosion frequently seems to cover the whole surface area of samples in a NaCl environment.

Some cavities have also been noted in addition to typical attack corrosion. It is believed that the corrosion in the case of samples in HCl is more akin to pitting corrosion than general corrosion. The microstructure was found to include many vacancies.

To view the samples' general microstructure, optical microscope photos are used. Overall, The findings presented visual representations obtained through optical microscopy of copper alloy samples following corrosion testing, with specific attention given to the examination of cavities within the material's structure.

Figure 4 shows the corrosion properties of copper alloys (CuSnSi alloy), optical microscope images after immersion in different solutions (HCl:1, NaCAL:6, NaOH:3 and NaOH:5) at various concentrations for a certain time, respectively (Şahin and Cantürk, 2022).

The results provided additional evidence that oxygen was generated within the black pitting regions of the samples, confirming their corrosion.

Furthermore, the presence of oxygen formation was observed even in areas without pits, suggesting the occurrence of overall or general corrosion (Şahin and Cantürk, 2022).

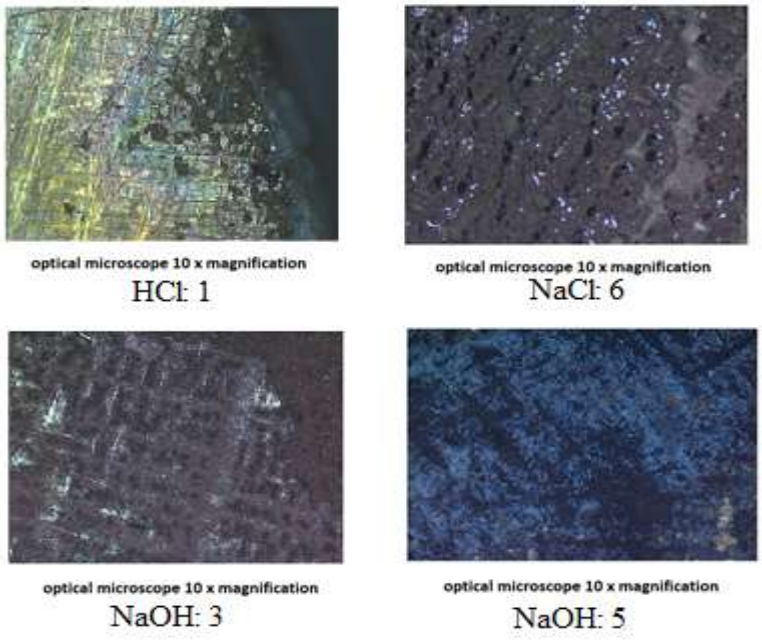


**Figure 4.** Corrosion Properties of Copper Alloys (CuSnSi alloy), Optical Microscope Images in Different Solutions (HCl:1, NaCAL:6, NaOH:3 and NaOH:5) (Şahin and Cantürk, 2022)

## 3. ChemiDoc™ MP IMAGING SYSTEM

The Bio Rad ChemiDoc imager (Figure 5) is a device with an intuitive touchscreen interface and best-in-class imaging capabilities for viewing and analyzing nucleic, protein, western, and blot gels as well as both chemiluminescence and fluorescence detection.

Multiplex fluorescent western blot is designed to meet the needs of chemiluminescence detection, general gel documentation applications and spotless technology imaging. The tool saves time and cuts down on waste by removing superfluous processes and allowing you to assess electrophoresis outcomes and transfer performance before western blotting.

With auto focus, auto exposure, and straightforward operation, it can quickly generate broadcast-quality photographs. It may be used for colourimetric gel and stain documentation as well as a variety of sample types or investigations that call for diverse detection techniques, including standard gel imaging (Cha & Kwon, 2018; D'Arcy et al., 2022).

Advanced sensor technology also provides exceptional resolution with optimal exposure, especially for weak and thick tape.

Additionally, it includes a variety of illumination options, automatically detects trays suited to certain applications, and modifies display settings accordingly. To conduct protein, DNA gel, and blot imaging, the instrument features conventional emission filters

In the presented experimental measurement, the ChemiDoc MP imaging instrument (Bio-Rad Laboratories Inc) was used to measure the intensities of particular protein bands. The system's software (Bio Rad) is utilized for signal detection and analysis.

According to the comments of the researchers, a research investigation was conducted to explore the connection between the prevalent essential microelements in circulation (zinc, iron and copper) and their primary linking proteins during the initial phase of infection of the new coronavirus outbreak (Covid-19) in 2019 (Nedic et al., 2022).

Through protein molecular shapes immunoblot analysis, it was found that diagnosed individuals exhibited elevated levels of proteinase-bound alpha-2-macroglobulin tetramer and albumin monomer compared to healthful people. Furthermore, it has been observed that zinc may play a role in facilitating the presence of optimal circulating protein forms in Covid-19 patients in this investigation (Nedic et al., 2022).

**Figure 5.** The Chemi Doc MP Imaging Instrument manufactured by Bio-Rad Laboratories, Inc. (www.bio-rad.com)

The study measured higher concentrations of zinc ions in infected subjects compared to healthy subjects. Additionally, the amount of zinc/albumin and zinc/alpha-2-macroglobulin were determined. Proteins were further investigated by albumin, alpha-2-macroglobulin, and non-reducing SDS-PAGE.

In figure 6, alpha-2-macroglobulin and albumin were obtained as the main band, while several molecular species were detected (Nedic et al., 2022).

The primary molecular form of alpha-2-macroglobulin was found to be the dimer (360 kDa), while the monomer form (180 kDa) was scarcely detectable. Additionally, there were multiple further molecular types with different densities and ratios observed.

In terms of albumin, when compared to monomer forms, healthy people showed a larger proportion of dimer forms, whereas infected individuals showed a relatively lower ratio of dimer to monomer forms. (Nedic et al., 2022).

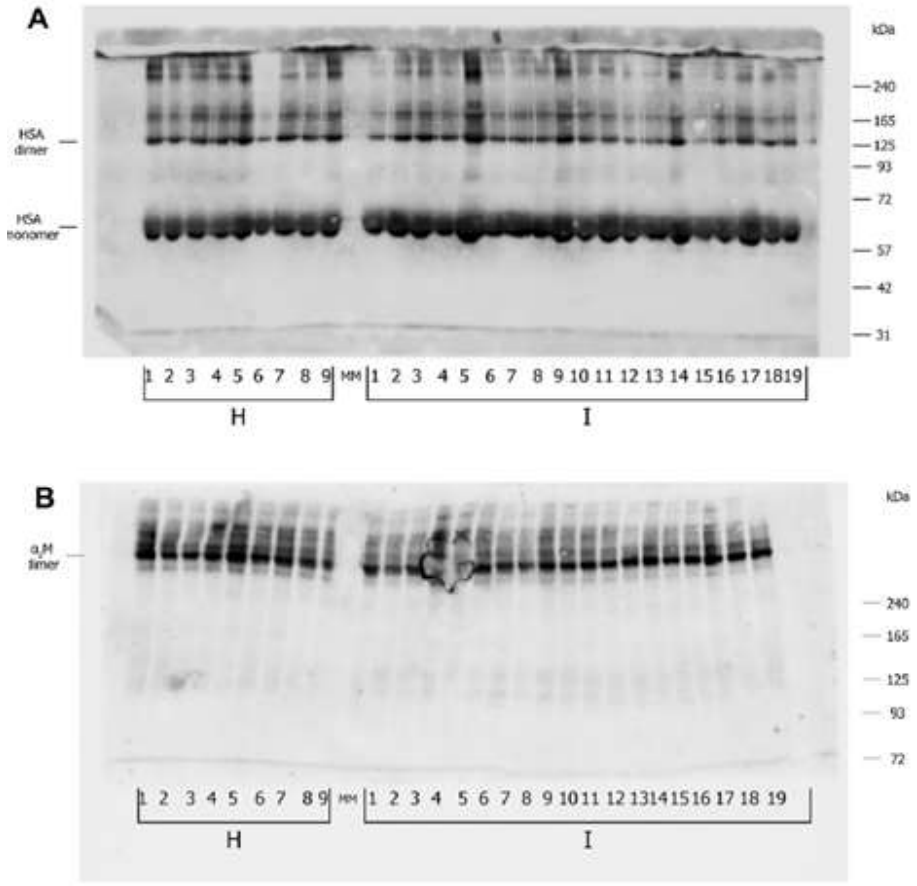


**Figure 6.** Following SDS-polyacrylamide Gel Electrophoresis, the Following Proteins were analyzed by Immunoblot in the Typical Samples (H-healthy, I-infected people): (A) Albümin –HSA, (B) Alpha-2-macroglobulin, respectively (Nedic, Sunderic, et al., 2022)

## 4. VIBRATING SAMPLE MAGNETOMETR CRYOGENIC LIMITED PPMS FOR VSM

Magnetic hysteresis measurement (VSM) is performed with the Cryogenic Limited PPMS (Physical Properties Measurement System) brand device (Figure 7).

The VSM measurement is employed to assess the magnetic characteristics of polymer-based powdered samples, both doped and undoped, within a defined range of magnetic fields. This characterization is conducted

either at room temperature or at a specific temperature value (Şahin, 2019; Ibrahim, 2015).

Vibrating Sample Magnetometer (VSM) and Superconducting Quantum Interference (SQUID) magnetometers are used for magnetic material characterization.

Basic magnetic parameters of materials such as magnetic field susceptibility (μ), saturation magnetization (Ms), residual magnetization (Mr) and coercive field (Hc) are determined by these devices.

VSM and SQUID magnetometers are calibrated using certified reference materials with known magnetization values, such as nickel and palladium. A closed-circuit Helium system is utilized to achieve extremely low temperatures, as low as 2 Kelvin (or -271 degrees Celsius), starting from room temperature (Şahin, 2019; Ibrahim, 2015; Bayrak, 2012).

Magnetic and electrical characterization of a certain amount of powder samples is made with a superconducting magnet capable of reaching magnetic fields as high as 5 Tesla.

Because of its vibrating sample magnetometer (VSM) and electrical measuring probes, this device can detect magnetic hysteresis, resistance and Hall effect, and alternating current (AC) susceptibility (Şahin, 2019; Şahin, Emek, et al., 2023; Sahin, Emek, et al., 2020; Ibrahim, 2015).

Below are our previous measurement results and analysis of a powder sample.

The magnetic features of CuO-doped $NiFe_2O_4$ samples, which were heat-treated at 1250 °C, were investigated at an ambient temperature (25 °C) via magnetic hysteresis examination conducted with a Cryogenic Limited PPMS instrument. The VSM investigation allowed for the characterization of the magnetic characteristics of Cu-doped and polyaniline-based nickel ferrite powder samples within a specific range of magnetic fields at ambient temperature (Şahin, Emek, et al., 2023).

The Cu-doped $NiFe_2O_4$:PANI composites' structure, composition, and magnetic characteristics are better-understood thanks to these investigations.

The magnetic features of CuO-doped $NiFe_2O_4$ samples, which were subjected to a heating temperature of 1250 °C, were evaluated at ambient temperature to investigate the influence of dopants on the magnetic characteristics. (Şahin, 2019; Şahin, Emek et al., 2023).

**Figure 7.** Cryogenic Limited PPMS Device for VSM (merlab.metu.edu.tr) (Şahin, 2019)

Figure 8a presents the magnetization of CuO-doped $NiFe_2O_4$ patterns based on the magnetic field (M-H), while Table 2 displays the calculated magnetic parameters of the samples. The sample with 0.1% CuO doping (x = 0.1) exhibited optimal ferromagnetic behavior, with a saturation magnetization (Ms) of approximately 41.8 emu/g. As the amount of Cu doping increased to x = 0.3, the saturation magnetization slightly raised to around 43.2 emu/g. However, when the Cu element ratio reached x = 0.5, the Ms value decreased to 36.5 emu/g. The observed trend suggests that the saturation magnetization increases with the addition of Cu element but decreases when the concentration reaches x = 0.5. The Neel's molecular field theory can explain the magnetization behavior of spinel ferrite, indicating that the exchange interactions between A-B sites are stronger than those between A-A and B-B sites (Şahin, Emek, et al., 2023).

When the CuO ions occupy B-sites at x = 0.1, it leads to a decrease in the amount of $Fe^{+3}$ ions at octahedral B-sites. This alteration in the magnetic structure results in a reduction in saturation magnetization. Additionally, the

dispersion of nonmagnetic CuO ions in both A and B sites may contribute to the decrease observed for $x \geq 0.5$. A slight decrease in Ms to 32 emu/g was observed when the $NiFe_{2-x}Cu_xO_4$ sample was doped with x = 0.6 CuO.

Saturation magnetization dropped as the PANI amount reduced from 1:1 to 1:3. As shown in Fig. 8b, the CuO-doped $NiFe_{2-x}Cu_xO_4$ samples (x = 0.1) with various Polyaniline quantities (1/3 and 1/1) exhibit magnetic area field-dependent magnetization at 1250 °C. Both samples displayed various ferromagnetic characteristics (Şahin, 2019; Şahin, Emek, et al., 2023).

With an amount of around 10.3 emu/g, the Ms for the specimen with a PANI content of 1/3 seemed smaller; in contrast, the specimen with such a PANI content of 1/1 displayed greater Ms with a valuation of roughly 22.7 emu/g. (Şahin, 2019; Şahin, Emek et al., 2023).

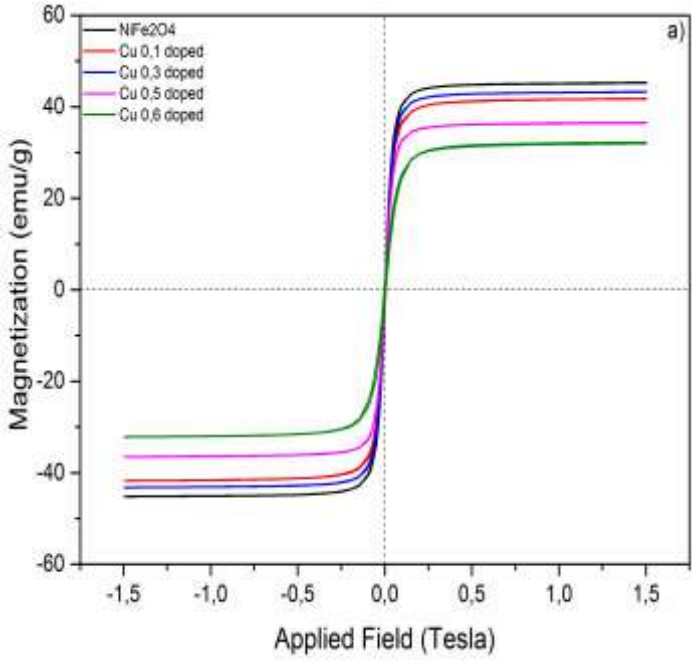

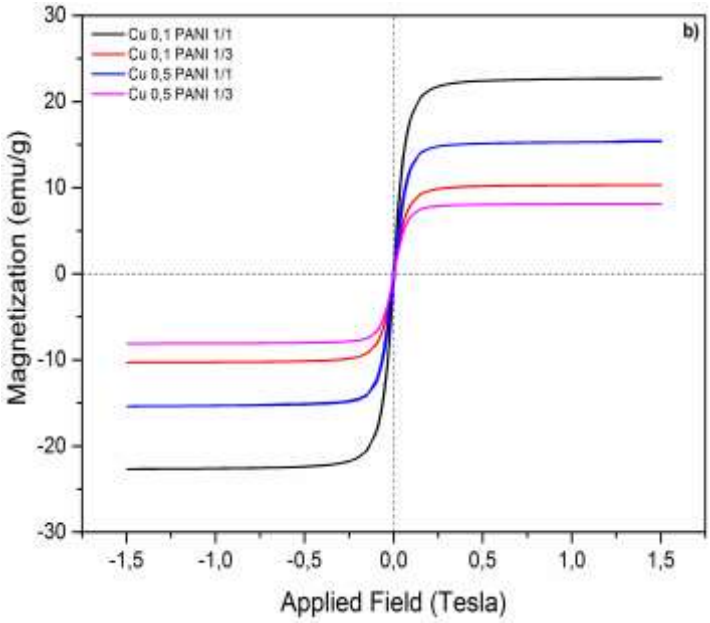


**Figure 8.** a) Magnetic Hysteresis Loops for Cu-doped $NiFe_2O_4$ (x= 0.1, 0.2, 0.3, 0.5) sintered at 1250 °C for 4 hours. b) Magnetic Hysteresis Loops for Cu-doped $NiFe_2O_4$ (x= 0.1, 0.5) using Polyaniline (1/3, 1/1) sintered at 1250 °C for 4 h (Şahin, 2019; Şahin, Emek et al., 2023)

A similar ferromagnetic activity was seen in CuO-doped $NiFe_{2-x}Cu_xO_4$ samples (x = 0.5) with differing Polyaniline amounts (1/3 and 1/1), in order of with Ms = 8.12 and 15.4 emu/g (Şahin, 2019; Şahin, Emek, et al., 2023).

In another study performed at low temperature, the VSM measurements of the Eu-doped $GdMnO_3$ compound were analyzed (Ibrahim, Mergen, et al., 2017)

To investigate the influence of dopants on the magnetic features, magnetic identification of the doped samples was carried out at low temperatures of 10K.

This allowed for a more detailed examination of how the presence of dopants affects the magnetic properties of the samples.

Figure 9 illustrates the relationship between the magnetic field (M-H) and magnetization of $Gd_{1-x}Eu_xMnO_3$ ceramics (x=0.2, 0.8) at low temperature (10K) (Ibrahim, Mergen, et al., 2017).

The x=0.2 sample, which has saturation magnetization (Ms) of around 35 emu/g, exhibits an astounding ferromagnetic activity.

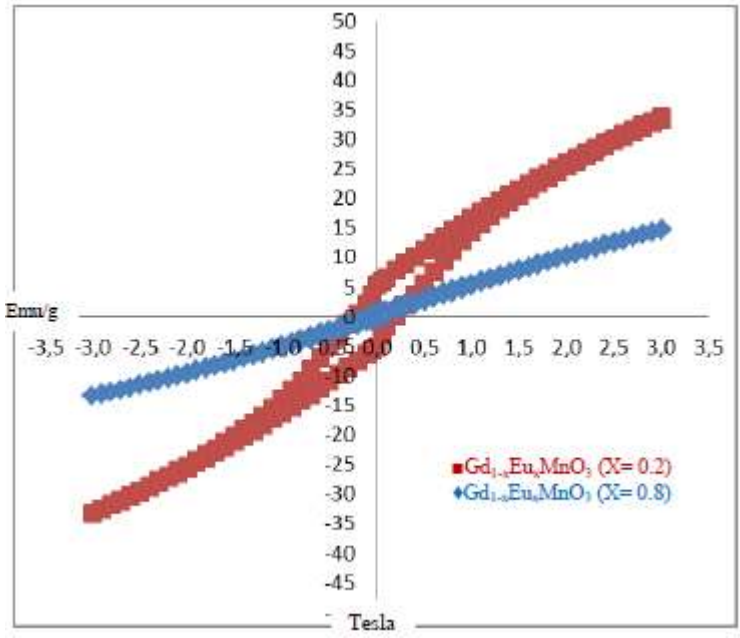


**Figure 9.** Magnetic Hysteresis Loops of $Gd_{1-x}Eu_xMnO_3$ samples (x=0.2 and 0.8) sintered at 1350 °C for 24h (Ibrahim et al., 2017)

With an increase in the dopant element concentration to x = 0.8, the magnetic feature undergoes a significant change from ferromagnetic to paramagnetic. This transition is accompanied by a decrease in the saturation magnetization (Ms) to approximately 14 emu/g.

The observed optimal ferromagnetic feature of the ceramic sample with x = 0.2 can be attributed to the effective suppression of the spiral spin modulation, which is achieved through the appropriate substitution of Eu ions. (Uniyal & Yadav, 2009).

However, when x exceeds 0.2, the introduction of dopants can lead to structural distortion, which disrupts the spin arrangement. As a result, the ferromagnetic behavior is compromised, leading to a noticeable reduction in the saturation magnetization (Ms) (Uniyal & Yadav, 2009; Ibrahim, Mergen, et al., 2017).

## 5. K-ALPHA X-RAY PHOTOELECTRON SPECTROMETER (XPS)

X-ray Photoelectron Spectroscopy (XPS) is a technique that detects characteristic electrons emanating from the surface of a sample (Figure 10).

XPS (X-ray Photoelectron Spectroscopy) is a technique utilized to analyze the photoelectrons emitted from the material's surface when it is exposed to X-rays. The kinetic energy of the photoelectrons released is determined, providing information about their binding energies within the parent atom. These binding energies are particular to the substance and its chemical configuration, allowing for the identification and analysis of elements present on the material's surface (Zhu et al., 2023; Göktürk, 2018).

XPS is an analysis technique used to provide atomic and molecular information about the surface of the material. Using XPS, it is possible to assess the oxidation levels of metals, the physical and chemical characteristics of materials, and the amount and quality of thin films (Göktürk, 2018).


**Figure 10.** K-Alpha X-ray Photoelectron Spectrometer (XPS) Device (thermofisher.com/xps-hub, www.thermofisher.com)

Dry samples of solids, powders and thin films can be measured. The technique is highly sensitive to the surface typical detection depth is ~5 nm on this device.

XPS can be used to determine the elements present on a sample surface, their relative concentrations or levels, and the total number of distinct elements present. It provides information on the film thickness and regularity if the substance is present as a thin layer on the surface (Göktürk, 2018).

XPS gives information about which elements are present on the sample surface, what levels of these elements are present, and how many of the different elements are present at different levels.

Besides, If the material is present as a thin layer on the surface, it gives information on film thickness and regularity. The most used application areas can be grouped under some main headings; polymer studies, microanalysis of the surfaces of metals and alloys, analysis of materials used for medical purposes, mineral surface studies, cement and concrete surface studies.

The most popular application fields may be categorized under a few major topics. Research on polymers, metals and alloys' surfaces are microanalyzed, examination of medically relevant materials, surface analyses of minerals, and surface analyses of cement and concrete.

In the study conducted by Zhu, Chen et al., XPS analysis was used to investigate the chemical states of CuPd catalysts and gain insights into their composition or makeup, X-ray photoelectron spectroscopy (XPS) has been used (Zhu et al., 2023).

CuPd bimetallic catalysts showed a positive shift in the Cu 2p peaks of 0.28 eV in comparison to Cu (Figure 11a), whereas the Pd 3d peak shifted to lower binding energy as Pd concentration increased (Figure 11b).

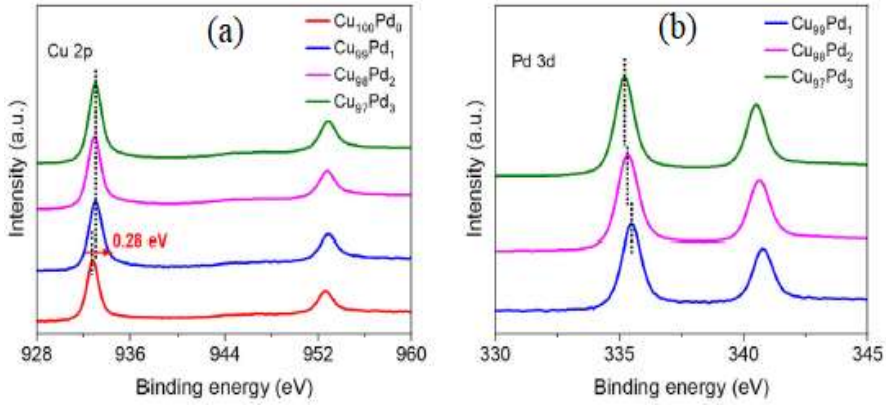


**Figure 11.** XPS spectra of several CuPd bimetallic catalysts ($Cu_{100}Pd_0$, $Cu_{99}Pd_1$, $Cu_{98}Pd_2$, $Cu_{97}Pd_3$) a) Cu 2p spectra b) Pd 3d spectra (Zhu et al., 2023)

Due to the interaction of Cu and Pd's electrons, there has been a minor shift in the binding energy of Cu 2p and Pd 3d.

The strong Cu $2p_{3/2}$ peak at 932.6 eV is also attributable to $Cu^0$ or $Cu^+$ species, and the Cu LMM Auger spectra further corroborated the presence of $Cu^+$ on the surfaces in addition to $Cu^0$. This oxidation may be related to the surfaces' exposure to air (Zhu, Chen et al., 2023).

Both Cu 2p and Cu LMM Auger peaks confirm that $Cu^0$ is the main species. $Cu^0$ is the main species, according to the Cu 2p and Cu LMM Auger peaks.

A two-part fit was made for the Pd 3d spectrum in catalysts.

Metallic $Pd^0$ is represented by the primary $3d_{5/2}$ peak at a binding energy of 335.4 eV, whereas $Pd^2$ in the $Pd^0$ state is represented by the extremely faint peak at 336.9 eV (Zhu et al., 2023).

## 6. ISOTOPE RATIO MASS SPECTROMETER (IRMS) DEVICE

Based on isotope ratios, isotope ratio mass spectrometry (IRMS) examines both natural and synthetic samples (Figure 12).

Depending on a material's source, origin, and any potential processes that could take place over its lifespan, its isotope ratio will change.

The isotope ratio mass spectrometry system enables laboratories to improve sample throughput, lower the cost per sample, and deliver extremely sensitive elemental and isotopic analysis.

The IRMS System offers multi-element elemental and isotope analysis at the g to mg level.

Additionally, this EA IsoLink IRMS System can integrate temperature-ramped gas chromatography and helium-saving technology, allowing for quick analysis times, cost-effective analysis, and excellent data quality, especially for small sample sizes.

In the disciplines of biology, ecology, archaeology, earth sciences, food integrity, and forensics, this equipment is utilized for regular examination and study.

Isotopic fingerprints (also known as isotopic signatures), which are left behind in food, fiber, liquid, or stone, can be used by researchers to identify origins, authenticity, and identity (Ehleringer, Bowen, et al., 2008; Bowen, 2010; Cerling, Barnette, et al., 2016)

**Figure 12.** Isotope Ratio Mass Spectrometer (IRMS) (DELTA$^{TM}$ Q, www.thermofisher.com,thermofisher.com/IsotopeFingerprints)

In previous studies, specific regions were selected and based on Local tap water. The study showcased the significant contribution that isotope fingerprints can provide in the field of human resource research. Water that is directly related to local-regional snowfall or precipitation but transferred between basins has been found to carry fingerprints for local regions derived from the hydrological cycle, which can also be affected in arid regions.

In the context of human movement from coastal areas to higher altitudes, the study revealed that there is a change in the isotope fingerprints of oxygen and hydrogen in precipitation. This change occurs because heavier isotopes are released from the clouds earlier than lighter isotopes. As a result, there is bound to be variation in $\delta 2H$ and $\delta 18O$ values between geographic regions, and this phenomenon is related to local-regional tap water (Ehleringer, Bowen, et al., 2008; Rodrigues, Brunner, et al., 2011; Bowen, 2010; Cerling, Barnette, et al., 2016).

Consequently, the researchers concluded that there is a significant relationship between the $\delta 2H$ and $\delta 18O$ values found in human hair and tap water. This finding establishes a robust framework for conducting human resource research using isotope analysis as a valuable tool. These results are based on bulk hydrogen and oxygen measurements using the Thermo Scientific™ EA IsoLink™ IRMS System Element Analysis Isotope Ratio Mass Spectrometer (Ehleringer, Bowen, et al., 2008; Rodrigues, Brunner, et al., 2011; Bowen, 2010; Cerling, Barnette, et al., 2016).

# 7. DIELECTRIC LCR METER (AGILENT E4980A)

Microwave dielectrics are materials that are employed in systems, including base station filter technology, mobile communication, and GPS navigation. Other technologies, including satellite technology and GPS antennas, also employ low-dielectric loss microwave dielectric materials (Şahin, 2010; Şahin, Emek, et al., 2023).

To be useful in this application, microwave dielectric materials must have high relative permittivity or dielectric constant, low dielectric loss or high-quality factor ($Q=1/\tan\delta$), and a resonance frequency temperature coefficient ($\tau_f$) that is almost zero.

Besides, microwave dielectrics must have strong temperature stability across a broad spectrum range and good mechanical and thermal stability.

In microwave dielectric materials, the quality factor Q is the inverse of the dielectric loss tangent ($\tan\delta$) and is an indicator of electrical energy loss in a dielectric system due to electrical conductivity, dielectric relaxation, and dielectric resonance.

The time difference between the vectors representing the electric field and the electric displacement may also be thought of as the cause of the dielectric loss (Şahin, 2010; Mergen, Eroğlu et al., 2010).

In the dielectric measurement example below, after the produced single-phase ceramics are sintered to a high density, both surfaces of the pellet are coated with silver or gold to determine their dielectric properties.

The coating process is carried out with another device, namely the Boc Edwards Auto 500 System brand coating device.

The pellets placed in the mask with a diameter of 5 mm are placed in the device and covered with pure silver.

After this process, contacts were taken from both surfaces using silver paste with silver wires with a resistance of 50 ohms, and the pellets adhered to a glass substrate of approximately 3 $cm^2$, one side of which was silver coated.

The samples placed in the vacuum chamber were kept for 1 hour at 200 °C and after cooling, they were kept under pressure between $10^{-2}$ and $10^{-4}$ bar for 4 hours and then measurements were started.

Our measurements were made with the Agilent E4980A Brand Precision LCR Meter at different temperatures (25°C-200°C) and frequencies (1 kHz-2 MHz) (Figure 13) (Şahin, 2010; Mergen, Eroğlu, et al., 2010; Şahin, Emek & Ibrahim, 2023).

The measurements conducted provided insights into the dielectric constant and dielectric loss as a function of frequency and temperature. Additionally, the temperature coefficient of the dielectric constant was calculated based on these measurements (Qasrawi, Şahin, et al., 2019; Şahin, 2023; Şahin, Emek & Ibrahim, 2023).

**Figure 13.** Dielectric Meter Device (Agilent E4980A Precision LCR Meter) (Şahin, 2010)

The dielectric constant temperature coefficient is calculated by the formula:

$$\alpha_{\varepsilon} = \frac{\varepsilon_{T_2} - \varepsilon_{T_1}}{\varepsilon_{T_1}(T_2 - T_1)}$$

In this formula, $\alpha_{\varepsilon}$ =dielectric constant is the temperature coefficient.

In addition, $T_2$ =120°C and $T_1$ =25°C, where $\varepsilon_{T_2}$ dielectric constant at 120°C , while $\varepsilon_{T_1}$ dielectric constant at 25°C (Şahin, 2010)**.**

The dielectric measurements of La-doped $Ba(Zn_{1/3}Nb_{2/3})O_3$ (BZN) structures, which are our own work, are described below.

The dielectric and dielectric loss spectra for the $Ba_{0.90}La_{0.1}(Zn_{1/3}Nb_{2/3})O_3$ perovskite ceramics, which were recorded in the temperature range of 20-200 $^{o}$C, are shown in Figures 14 a, b (Qasrawi, Sahin et al., 2021).

Figures 14a and 14b clearly show that increasing the signal frequency at a specific temperature results in an increase in both the dielectric constant and the dielectric loss tangent.

At a fixed frequency, when the temperature is raised, both the loss tangent and the dielectric constant decrease until they reach a certain temperature, and then they begin to rise with rising temperature.

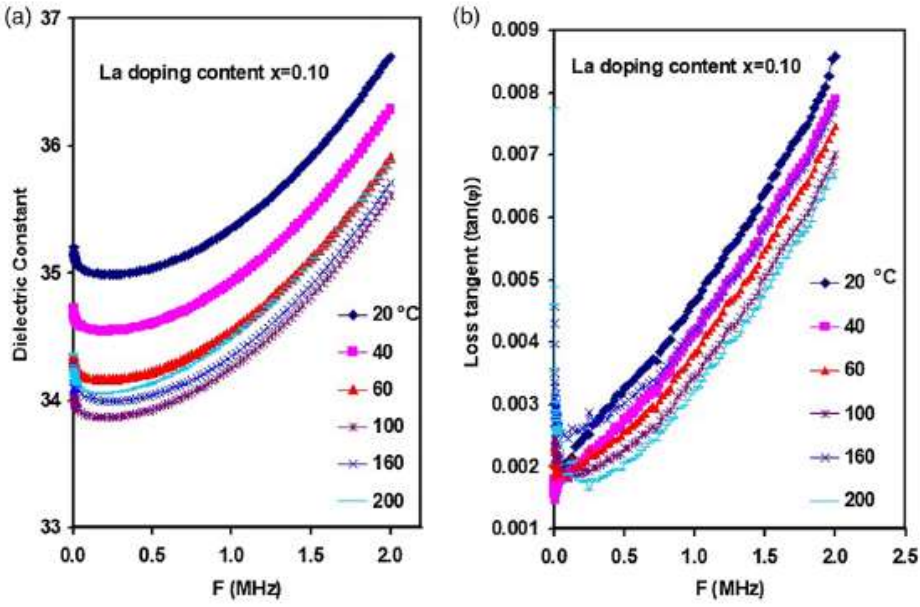


**Figure 14.** a) The Dielectric Constant and b) The loss tangent spectra for $Ba_{1-x}La_x(Zn_{1/3}Nb_{2/3})O_3$ solid solutions being detected in the temperature interval of 20–200 °C (Qasrawi, Sahin et al., 2021)

In Figures 15a and 15b, this phenomenon is depicted, respectively. Figure 15a,b shows two places where the temperature varies.

In simpler terms, the values of the dielectric constant (r) decrease as the temperature increases up to 120 °C. However, beyond 120 °C, the dielectric constant values start to increase again as the temperature continues to rise within the range of 140-200 °C.

At signal frequencies of 1.0 kHz and 2.0 MHz, the loss tangent exhibits a decreasing trend with fluctuations within the temperature range of 20-120 °C. However, it reaches its peak values at critical temperatures of 140 °C and 160 °C (Qasrawi, Sahin, et al., 2021).

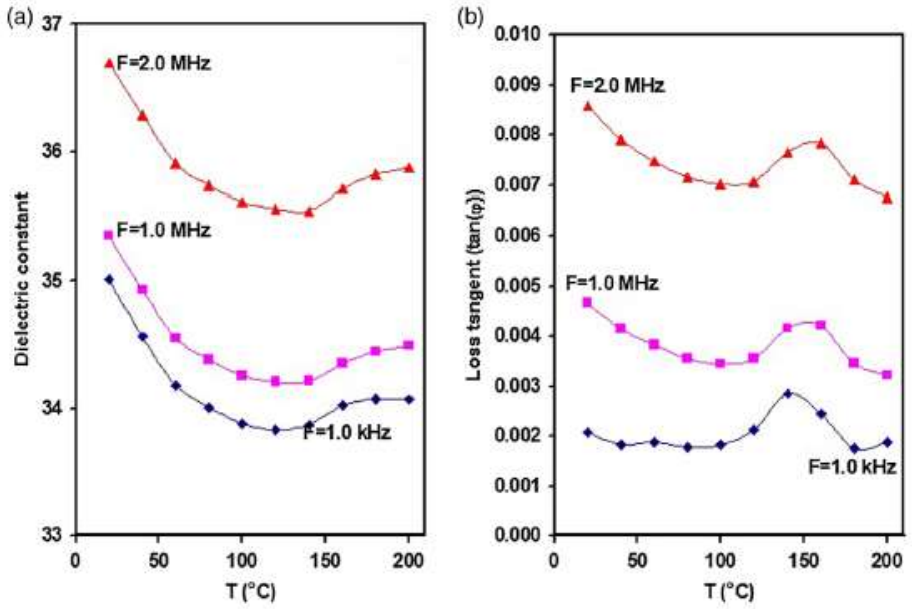


**Figure 15.** The Temperature Dependencies of a) Dielectric Constant and b) Dielectric Loss Tangent for $Ba_{0.9}La_{0.1}(Zn_{1/3}Nb_{2/3})O_3$ Solid Solutions (Qasrawi, Sahin et al., 2021)

It is believed that the presence of dielectric relaxation in the doped BZN (bismuth zinc niobate) samples are responsible for the shifting of the critical temperature to higher values as the frequency increases.

The explanation for the increase in dielectric constant value with increasing frequency and temperature in the high-temperature range involved the utilization of the Maxwell-Wagner (MW) type of interfacial polarization and Koop's theory of dielectrics. These theories provided an understanding of the underlying mechanisms contributing to the observed behavior (Qasrawi, Sahin, et al., 2021).

The MW type of polarization is specifically utilized to describe the polarization behavior occurring at the interfaces or boundaries between grains (clusters of crystallites) in the low-frequency range. This model is commonly employed for studying inhomogeneous materials, which include multiphase materials and materials containing numerous interfaces and defects (Qasrawi, Sahin, et al., 2021).

Within the MW type of polarization model, the dielectric loss contribution can be substantial in comparison to the dielectric response originating from molecular fluctuations. This is because charges are often separated over a large area, extending beyond the atomic and molecular dimensions. As a result, the interactions at interfaces or boundaries play a crucial role in the dielectric behavior of the material (Rodon et al., 2018).

The rise in AC conductivity $(\sigma = \varepsilon_r \omega \tan(\delta))$ values, on the other hand, is followed in a high-frequency zone by grains that have a conductivity that is substantially greater than grain boundaries, in accordance with Koop's theory of dielectrics.

Conductivity readings that change slowly or remain constant are caused by grain boundaries with high resistance in the low-frequency range (Rodon et al., 2018).

For researchers, the effects of the secondary phases formed in the material structure on the dielectric properties can be investigated in detail. The optical properties of doped materials can be studied. Microwave dielectric properties of single-phase doped materials can be determined at high frequencies. By measuring the electrical properties of the doped materials, how the additives affect the electrical and dielectric properties can be examined in detail.

## 8. TG–DTA DEVICE (THERMO GRAVIMETRIC-DIFFERENTIAL THERMAL ANALYSIS)

Thermal characteristics of materials, including mass changes, activation energies, glass transition temperatures, boiling and melting points, specific heat, reaction kinetics, and thermal stability, may be investigated using the TG/DTA Device (Figure 16).

Thermogravimetric Analysis (TGA) is a method that involves tracking the mass of a sample based on temperature or time within a regulated temperature program in a controlled environment.

A typical TGA setup consists of a sample pan that is placed on a precision balance.

Throughout the experiment, an oven-based pan is heated or chilled. Throughout the experiment, the sample's mass is tracked. The sample environment is managed by a gas used for samples (Ayanoğlu, 2019; Gümüş, 2010).

This gas might be an exhaust gas or an inert gas passing over the sample.

To raise the temperature as much as required at desirable times, the furnace in the system may be designed to operate between 25 and 1100 °C.

TGA can operate up to 1100 °C in temperature. DTA can be performed at lower temperatures compared to TGA, typically up to 500 °C. Various materials exhibit distinct melting and sublimation temperatures, undergo mass loss or gain, and experience phase changes and oxidation-like characteristics may all be calculated using the TGA-DTA apparatus (Gümüş, 2010; Ayanoğlu, 2019).

In actuality, this technique simultaneously measures both the temperature difference and the weight change between the sample and the reference.

It is possible to identify phenomena involving mass change, thermal stability, enthalpy of transformation, specific heat, glass transition temperature,

**Figure 16.** The Thermogravimetry (TG) and Diffrential Thermal Analyzer (DTA) Device, NETZSCH STA 449 Jupiter Model (www.netzch.com, analyzing-testing.netzch.com/en/media/brochure)

crystallization behavior, decomposition, dehydration, oxidation, pyrolysis, reduction, adsorption, and desorption in the samples (Mergen, Eroğlu, et al., 2010).

In the chemical and pharmaceutical sectors, TGA is a popular analytical technique. Analyses can be conducted on a variety of materials, including clay and minerals, metals and alloys, food, medicines, polymers, rubber, coatings, adhesives, and pharmaceuticals.

Finding the filler or fiber content in polymer and composite materials is one of the TGA device's most crucial application areas.

It is frequently utilized in quality control and research and development projects for a variety of industrial goods.

In the sample measurement below (Figure 17), TG/DTA analysis was carried out. (Mergen, Eroğlu et al., 2010).

With the citrate gel method, BZN-3 samples with a mole ratio of citric acid/total metal cation of 1 were firstly examined using DTA-TG after being subjected to 2h heat treatment at 300°C (Mergen, Eroğlu, et al., 2010).

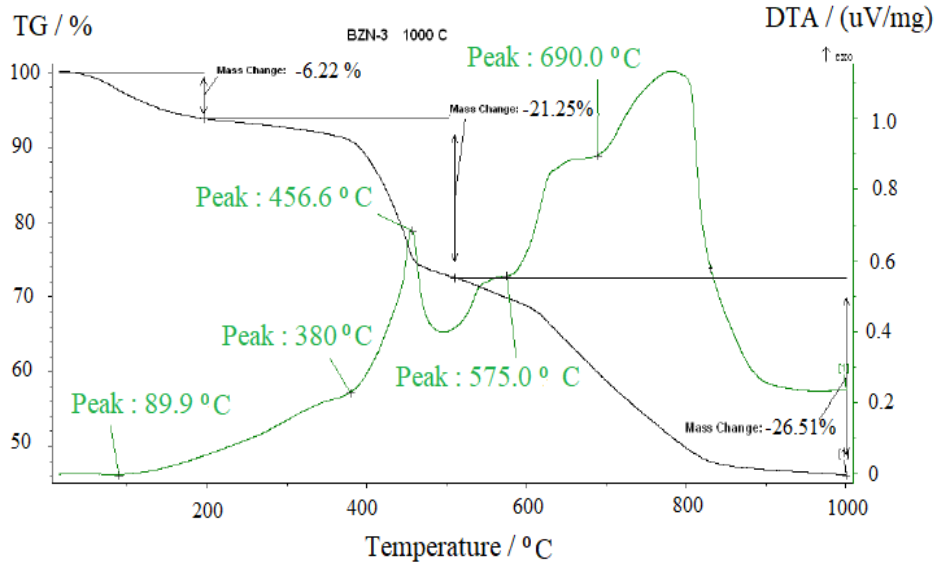


**Figure 17.** Differential Thermal Analysis (DTA) and Thermogravimetry (TG) Curves of BZN-3 Powder (Mergen, Eroğlu, et al., 2010)

BZN is $Ba(Zn_{1/3}Nb_{2/3})O_3$ in this investigation.

BZN-3 powder exhibits a 54% overall weight loss up to 1000°C, as seen by the TG curve (Figure 17).

The evaporation of adsorbed water on the powder surface of BZN-3 is likely the cause of the approximately 6% weight loss that occurs in the 20–200°C range; an endothermic peak corresponding to this loss of weight was generated at 90°C.

With the exception of the 6% weight reduction, both stages resulted in an overall weight decrease.

The temperature ranges for these stages are 200–510°C and 510–1000°C, respectively, and the weight loss in the first and second stages is around 22% and 25%, respectively.

According to how the previous DTA-TG curves were interpreted, the organic matter's decomposition in the first stage is what caused the 22% weight loss (Mergen, Eroğlu, et al., 2010).

The endothermic peak at around 380 °C and then the exothermic peak at around 457 °C are due to the decomposition of organics and the resulting combustion of carbon.

The second major weight loss of 25% is probably due to the decomposition of organics and $BaCO_3$ remaining in the system and the evaporation of ZnO, resulting in endothermic peaks at approximately 575 °C and 690 °C (Mergen, Eroğlu, et al., 2010).

## 9. FTIR DEVICE

It is a significant spectroscopic method employed to acquire infrared absorption and transmittance spectra of both solid and liquid samples.

FTIR utilizes infrared energy to excite the atoms in a material. By measuring the spectrum of light absorbed and transmitted as the atoms vibrate, FTIR spectroscopy provides a unique fingerprint of the molecular structure and composition of the sample (Şahin, 2019).

This fingerprint can be used to identify chemical bonds present in the sample.

FT-IR analysis was conducted using a NICOLET device infrared spectrometer, which utilizes Fourier transform technology to obtain infrared spectra (Şahin, 2019).

In the wavelength range of 4000-500 $cm^{-1}$, at room temperature against % transmittance, placing the doped powder samples on the sample holder was accomplished by absorbing the infrared light by the sample (Şahin, 2019).

By analyzing with FTIR (Fourier transform infrared) spectrometer (Figure 18), it is understood that peaks occur in different wavelength ranges.

The sending of infrared radiation on the sample and the vibration movements of the chemical bonds in the sample in different ways and the absorption of infrared radiation create spectral peaks.

When an infrared beam is sent, the molecules absorb the beam only at their vibrational frequency.

Various characteristic peaks of powdered compound samples were analyzed, and valuable insights into the chemical bonding within the structures were obtained.

**Figure 18.** FT-IR Spectrometer Device (Nicolet™ İs20) (www.thermofisher.com)

Figure 19 shows the results of an FTIR study of $ZnNb_2O_6$ powders made using a citric acid/metal oxide ratio of 1 that were charred at 300 °C and heated for two hours at various degrees (400–1000 °C) (Mergen, Eroğlu, et al., 2010).

It is believed that the metal-oxygen stretching vibrations in the $ZnNb_2O_6$ structure are what cause the absorption bands seen in ZN-1 powders at about 600 and 800 $cm^{-1}$.

Due to the amorphous nature of the powders, these lines begin to appear at 400 and 500 °C and become finer as the temperature increases (Mergen, Eroğlu, et al., 2010).

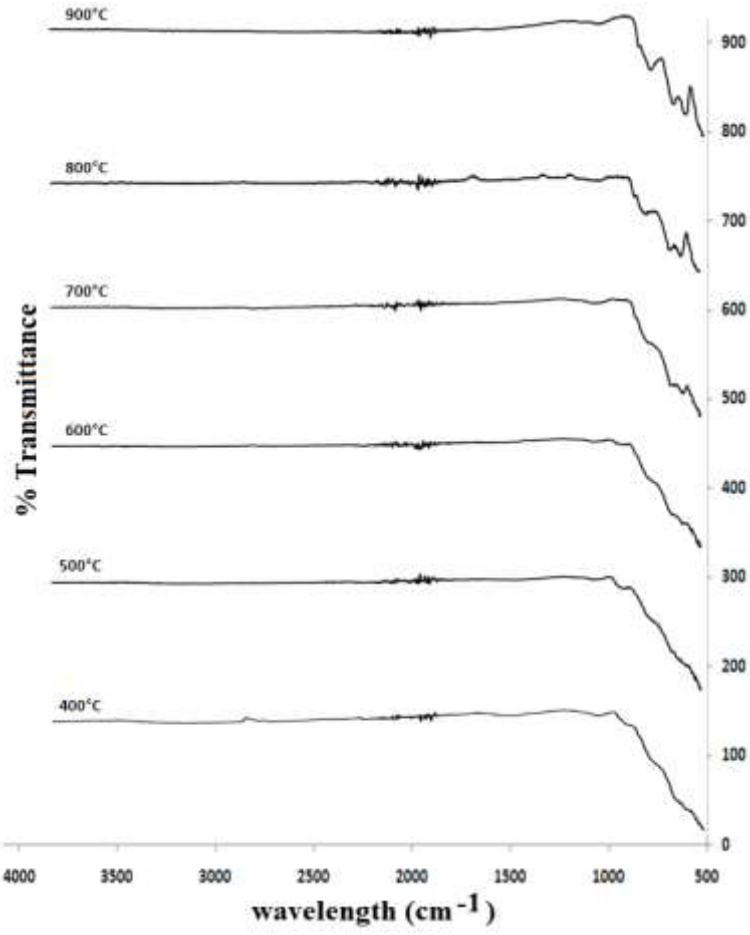


**Figure 19.** FTIR Spectra of $ZnNb_2O_6$ Powder Produced as Citric acid/metal Oxide Ratio:1 and Charred at 300°C after 2 hours of Heat Treatment at Different Temperatures (Mergen, Eroğlu et al., 2010)

In a separate sample measurement, the spectra shown in Figure 20 displayed characteristic absorption peaks less than 600 $cm^{-1}$ for all the ceramic samples. These peaks can be assigned to the stretching vibrations of the Ni-O bond or Fe-O in $NiFe_2O_4$, indicating the presence of these bonds in the material. (Şahin, 2019).

The occurrence of spectral peaks at approximately 1473 and 1552 $cm^{-1}$ in the doped PANI samples suggests the polymerization of aniline. These peaks correspond to the stretching modes of C=C and C=N, respectively, for the quinonoid and benzenoid units of PANI (Şahin, 2019).

Specifically, for the HCl-doped PANI, these peaks confirm the presence of polymerized aniline units in the material (Khairy, 2014).

The peaks observed at 1236 $cm^{-1}$ and 1239 $cm^{-1}$ in the PANI-containing samples can be attributed to the C-N stretching of the benzenoid ring. Additionally, the characteristic peak at 1289 $cm^{-1}$ in all the PANI samples is assigned to the C-N stretching mode of the benzenoid units. These spectral features provide further evidence of the presence of PANI and its specific molecular structure in the samples (Şahin, 2019).

The stretching vibrations observed at specific wavenumbers, such as the peaks at 1236 $cm^{-1}$ and 1239 $cm^{-1}$, can be attributed to the stretching vibrations of metal-oxygen bonds at the tetrahedral and octahedral sites, respectively. Additionally, the peak at 1289 $cm^{-1}$ corresponds to the stretching of C-N bonds in secondary amine groups within the polymer main chain. These spectral assignments provide insights into the bonding and structural characteristics of the material under investigation (Baykal, Günay, et al., 2013; Khairy, 2015; Khairy & Gouda, 2018).

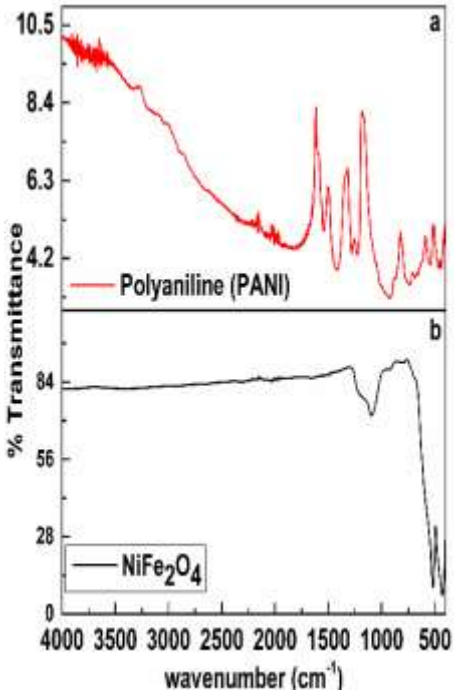


**Figure 20.** FTIR Spectra of Analysis of PANI-$NiFe_2O_4$ a) Polyaniline b) $NiFe_2O_4$ (Şahin, 2019)

## 10. X-RAY DIFFRACTION (XRD) DEVICE (BRUKER D2 PHASER DIFFRACTOMETER)

A crystal's atomic planes cause the incoming X-ray beam to interfere with each other as it exits the crystal. X-ray diffraction is the term for this phenomenon.

This instrument is an analytical method that provides details about different crystal forms or phases in the structures of solid and powder samples.

It is also often used to determine the phase of a crystalline substance and provides details on the unit cell's size and the periodic arrangement of atoms in the unknown crystal sample's lattice (atomic spacing and crystal structure) ( Şahin, 2019; Şahin, 2010).

XRD analysis is a potent, non-destructive technique used to identify the crystalline phases that are present and provide information on the concentration of these phases, the amount of non-crystalline phases, the crystal size, and ultimately the chemical composition (Topcu, 2020; Topcu, 2022; Topcu, Ceylan, et al., 2020; Şahin, Emek, et al., 2023; Şahin, 2022; Şahin, 2023).

The important benefits of X-ray diffraction are: It is a quick and effective method for detecting unidentified minerals and materials.

The collected data are compared to the data in the reference database to identify the phases.

Only a little sample has to be prepared for analysis. The data that is produced may be interpreted pretty simply (Şahin, 2010; Şahin, 2019; Ibrahim, 2015).

In the conducted sample measurement, the sintered pellets were crushed into a powder using an agate mortar. The resulting powder was then placed on a sample holder and analyzed using X-ray diffraction (XRD). This analysis aimed to determine the solubility limit of each additive in the sintered pellets and identify any secondary phases that may have formed.

The doped sintered samples were characterized for their phases using X-ray diffractometry. The measurements were performed using a Bruker D2 Phaser apparatus, and Cu-Kα radiation with a wavelength of 1.5406 Å was used. The scanning range was set from 2θ: 10-70°, with a scanning rate of 1 degree per minute. The purpose of this analysis was to quickly scan and identify the phases present in the doped sintered samples (Şahin, 2019; Şahin, 2010).

The solubility limit of a certain component, which represents the maximum amount that can be added to a material (in this case, $NiFe_2O_4$)

without causing any phase changes in the basic structure, was identified using X-ray powder diffraction.

The results are depicted in Figure 21, which provides information about the composition range within which the main structure remains unaffected by the addition of the component.

In the use of the device, when the X-ray is sent on the crystal, it is scattered from the atoms in the crystal, and when the X-ray is high, the intensity increases; that is, when the peak intensity increases, the diffraction is high.

The graph of the angle of the incident X-rays corresponding to the intensity is obtained.

This intensity peak seen in the graph gives us information about atoms and compounds.

By sending X-rays, the scattered rays on the sample show a certain intensity; these intensity peaks are observed by changing the angle of the incoming ray. Information about the crystal atoms in the compound could be obtaıned (Şahin, 2019; Qasrawi, Sahin, et al., 2021).

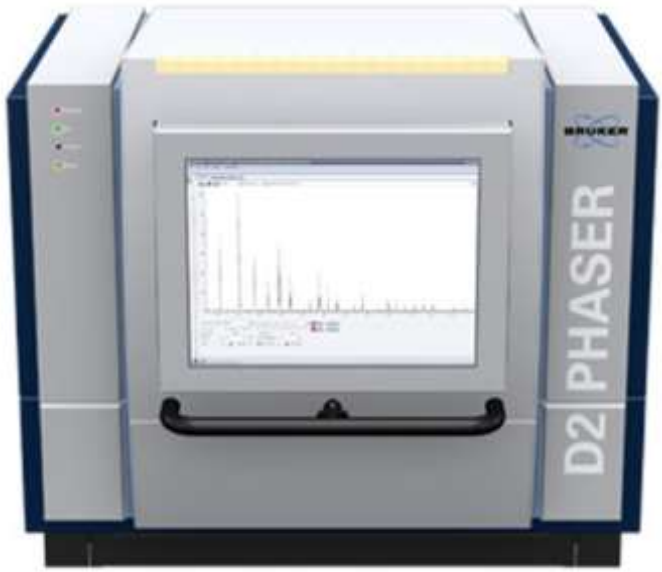


**Figure 21.** X-RAY Diffraction (XRD) –Bruker D2 Phaser (Şahin, 2019; Şahin, 2010)

In our XRD review below, the measurement results are included with the comments.

$Ba(Zn_{1/3}Nb_{2/3})O_3$ is (BZN) (Şahin, 2010).

The empirical formula $Ba_{1-x}La_x(Zn_{1/3}Nb_{2/3})O_3$ is used to evaluate lanthanum doping in barium sites in the current work.

$La^{+3}$ has an ionic radius of 1.36 Å, which is lower than $Ba^{+2}$'s (1.61 Å ) and greater than $Zn^{+2}$'s (0.74 Å ) and $Nb^{+5}$'s (0.64 Å ).

This characteristic limits the substitutional doping of lanthanum in barium-containing locations.

Figure 22 shows the X-ray diffraction (XRD) patterns obtained for the samples with varying La contents ranging from 0.02 to 0.20 (Qasrawi, Sahin et al., 2021; Şahin, 2010).

Software tools called "TREOR 92" are used to evaluate the obtained XRD peaks that in pure materials exhibit their highest reflection at diffraction angles of $2\theta = 31.10°$ (Qasrawi, Sahin, et al., 2021; Şahin, 2010).

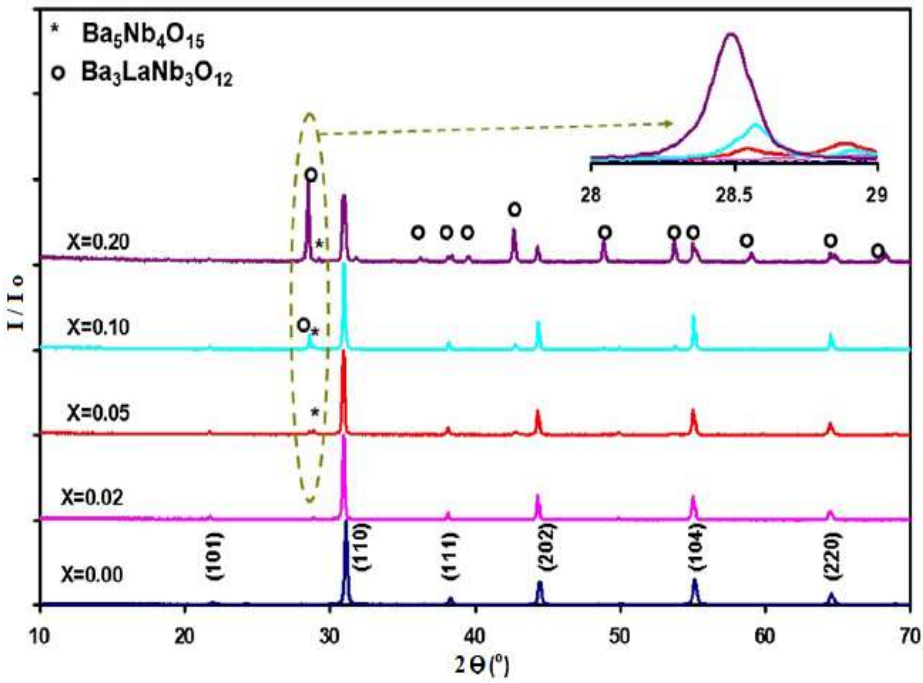


**Figure 22.** The La-doped $Ba(Zn_{1/3}Nb_{2/3})O_3$ Ceramics' XRD Patterns. The Peaks of Minor Phases are shown in Inset 1 (Qasrawi, Sahin, et al., 2021; Şahin, 2010)

The lattice constant (a) of a cubic lattice with these peaks was 4.065 Å.

The (110) direction is preferred by pure perovskite ceramics for planar orientation.

Between the theoretically estimated peak positions according to the software package and the thorough experimentation observed peak positions, there is an error of less than 1.0%.

Miller indices and the computed lattice parameter agree with published data (Qasrawi, Sahin, et al., 2019) and JCPDS Card No. 17-182 for pure $Ba(Zn_{1/3}Nb_{2/3})O_3$.

In Figure 23a, the highest peak of perovskite ceramics is shown based on doping concentration. The figure illustrates that lanthanum doping has a significant effect on the peak position, shifting it towards lower diffraction angles.

The observed shift in the XRD peaks indicates an increase in the lattice constants, suggesting that the addition of lanthanum modifies the crystal structure and leads to the expansion of the perovskite ceramics lattice.

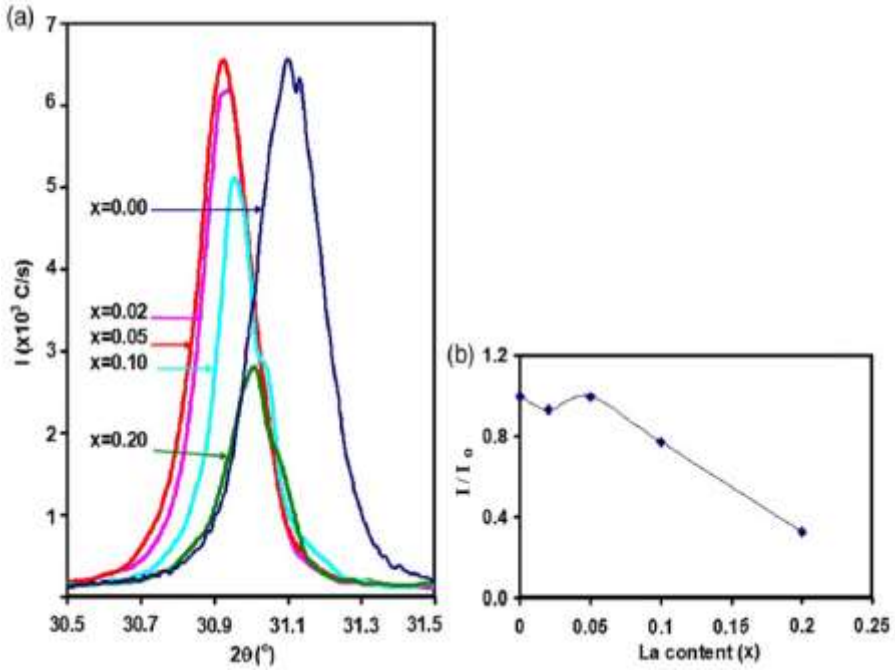


**Figure 23.** a) As a Function of La Concentration, the Shift in the Maximum Reflection Peak of the BZN, and b) As a Function of Doping Content, the Change of Normalized Doped Maximum Peak Intensity (Qasrawi, Sahin et al., 2019)

The lattice shrinkage of matrix crystals is often brought on by smaller ion doping, in contrast to what has been seen here.

Perovskite oxide systems like $Pr^{x}_{1-x}Sr^{'}_{x}B^{x}_{1-x}B^{\circ}_{x}O_3$ have also been reported to exhibit comparable characteristics to those found here.

It was explained by an increase in the amount of $B^{+3}$ cations and a decrease in the amount of $B^{+4}$ cations.

According to Pauling's second rule, a drop in $B^{+4}$ cations resulted in a fall in the strength of the B-O bond. Due to the $BO_6$'s expanding size, the lattice must enlarge (Kostogloudis, Fertis, et al., 1998).

Doping with elements of lower ionic radii can lead to the creation of oxygen vacancies at high temperatures, which is another factor contributing to lattice expansion. (Arshad, Azam, et al., 2011).

The XRD intensity noticeably drops along with the change in peaks, as seen in Figure 23b.

Due to the disorder caused by La or the doping-induced deterioration of crystallinity, the XRD peaks' intensities decrease (Liu, Hou, et al., 2019).

Figure 22 also makes it evident that additional peaks began to form after La doping, with rising La concentration.

The inset of Figure 22 shows a close-up view of the XRD diffractogram of the doped samples, specifically highlighting the appearance of a small peak near a diffraction angle of $2\theta = 28.57°$.

With increasing doping concentration, the inset in the figure shows that the peak becomes sharper and shifts towards smaller angles.

In an effort to determine the cause of the new peaks that started to develop in samples with a La content of x=0.05, $Ba_5Nb_4O_{15}$ was found to be present as a minor phase.

The measured peaks for La concentrations of $0.05 \leq x \leq 0.20$, which are depicted in the inset of Figure 22, were consistent with those of $Ba_5Nb_4O_{15}$ (JCPDS Kart No: 14-028).

Figure 22 shows that new peaks, indicated by open circles, appeared when the La contents were increased to x = 0.10.

$Ba_3LaNb_3O_{12}$ (JCPDS Kart No. 44-929) was found to be connected to these peaks.

It shows that the solubility cap for La doping to BZN has been surpassed.

In the BZN samples doped with La at x=0.05, the phase weight of $Ba_5Nb_4O_{15}$ is 2.7%.

$$Ba_5Nb_4O_{15}\ \left(\frac{\sum I_{Ba5Nb4O15}}{\sum I_{all\ peaks}}\right)$$

The minor phase weight increased to 7.6% when x = 0.10 doping concentration. With a phase weight of 60.47%, the second minor phase ($Ba_3LaNb_3O_{12}$) dominates at x = 0.20.

BZN is lost as a result, and new material is created.

Based on X-ray analysis, it was found that the solubility limit of La in the perovskite ceramics was reached at relatively low concentrations, specifically at x = 0.02.

In another study of ours, the XRD examination of the dope compound is given below.

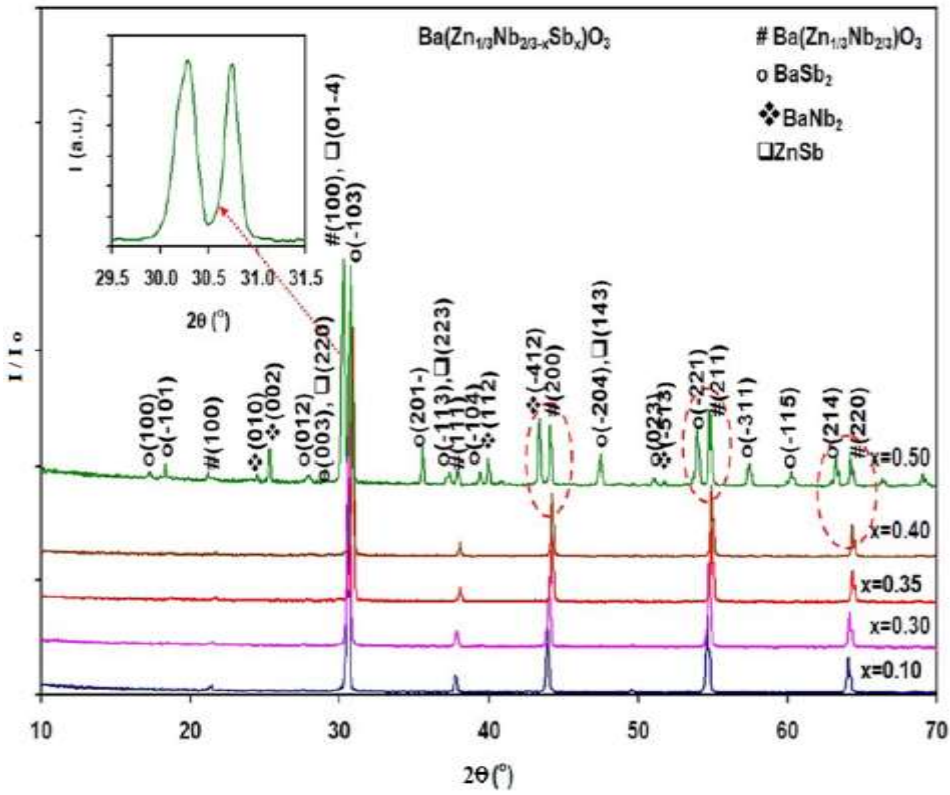


**Figure 24.** Sb doped BZN Ceramics Sintered for 4 hours at 1400°C with x=0.1,0.3, 0.35, 0.4, and 0.5 are Shown in the XRD Patterns (Şahin, 2010; Qasrawi, Sahin et al., 2019)

In $Ba(Zn_{1/3}Nb_{2/3})O_3$ compound, Sb element is doped by using $Ba(Zn_{1/3}Nb_{2/3-x}Sb_x)O_3$ composition instead of Nb because its ion diameter is close to Nb cation (Figure 24). In this formulation, the x value was taken as 0.1, 0.3, 0.35, 0.4 and 0.5. The produced compositions were sintered at 1400 °C for 4 hours for XRD analysis.

Cubic crystal phases with the most intense surfaces orientated in the (110) direction were revealed through a study of the XRD patterns.

New structures were formed when the Sb concentration in the BZN was increased to x=0.5.

However, when the doping concentration reaches x = 0.5, secondary phases are observed in the structure.

This indicates that the solubility limit of the Sb element in the Sb-doped BZN ceramics sintered at a temperature of 1400 °C is x = 0.4.

It was observed that the XRD peaks of the BZN perovskite phase were bifurcated and formed as double peaks at the x=0.5 contribution.

This is because, at x=0.5 doping ratio, high doping distorts the structure, transforming the BZN cubic perovskite structure into a crystalline structure with lower symmetry.

As depicted in the inset of Figure 25, the peak observed at a diffraction angle of $2\theta = 30.59°$ splits into two separate peaks.

When the Sb ratio is raised to x=0.5, all other peaks that are visible in samples that have been doped with Sb at concentrations of $0.10 \leq x \leq 0.40$ also break into two peaks (Şahin, 2010; Qasrawi, Sahin, et al., 2019).

The single-phased BZN (Figure 25 (a)) lost its distinctive cubic structure and largely disintegrated into hexagonal ZnSb (Figure 25 (b)), monoclinic $BaSb_2$ (Figure 25 (c)), and monoclinic $BaNb_2$ (Figure 25 (d)), all of which have lattice parameters of a=10.218, b=3.630, c=8.315 Å and β=120.03°.

The initially single-phased BZN material, as depicted in Figure 25 (a), undergoes significant structural changes and decomposition. It transforms into different crystalline phases, including hexagonal ZnSb with lattice parameters a=12.131 Å, b=12.131 Å, c=12.351 Å, and β=120.0° (Figure 25 (b)). Additionally, it decomposes into monoclinic BaSb2 with lattice parameters a=5.176 Å, b=4.357 Å, c=9.431 Å, and β=101.55° (Figure 25 (c)), as well as monoclinic $BaNb_2$ with lattice parameters a=10.218 Å, b=3.630 Å,

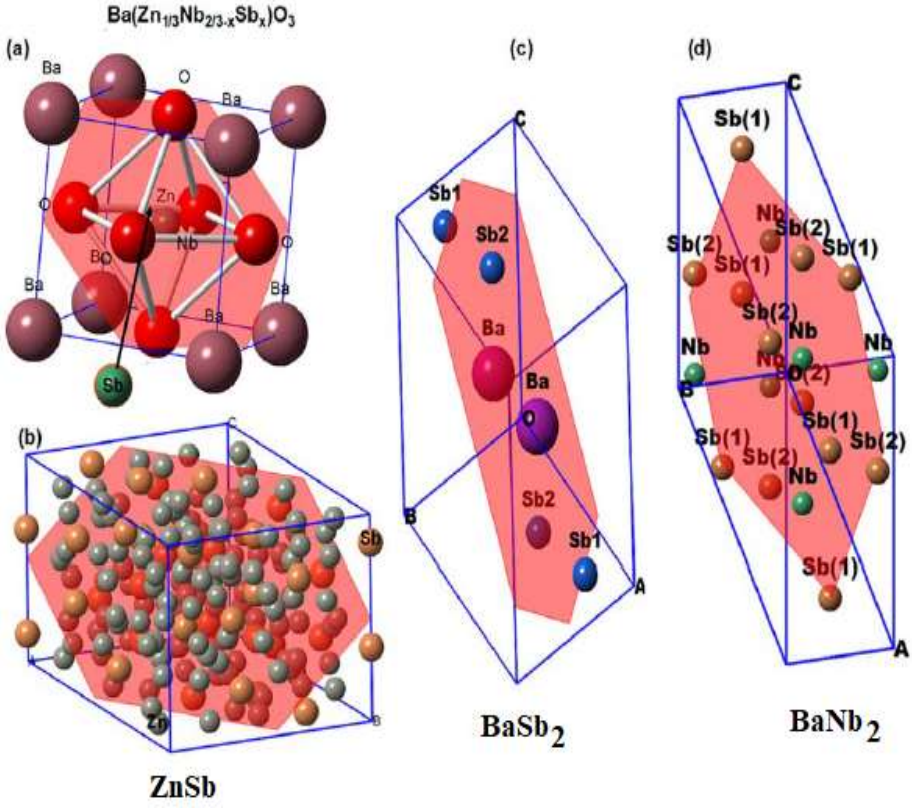


**Figure 25.** The Diagrams for (a) Perovskite $Ba(Zn_{1/3}Nb_{2/3-x}Sb_x)O_3$, (b) ZnSb, (c) $BaSb_2$, and (d) $BaNb_2$ crystals (Qasrawi, Sahin, et al., 2019)

c=8.315 Å, and β=120.03° (Figure 25 (d)). These structural transformations indicate the complex nature of the decomposition process and the formation of different crystalline phases in the BZN material.

The lattice parameters of the material align with the values reported in the Crystallography Open Database (COD) cards, specifically COD numbers 7040 425 for $BaNb_2$ and 8100 903 for $BaSb_2$. (Şahin,2010; Qasrawi, Sahin et al., 2019).

These three phases are found in the structure of BZN, which shows that the material's solubility limit has been surpassed and further doping is useless.

The 'Crystalmaker' software tools also show how the high doping of Sb leads to the decomposition of the cubic structure of $Ba(Zn_{1/3}Nb_{2/3})O_3$.

Figure 25 (a) shows the computer simulation schematics for $Ba(Zn_{1/3}Nb_{2/3})O_3$ before doping, whereas Figures 25 (b), (c), and (d) depict the schematics for hexagonal ZnSb, monoclinic $BaSb_2$, and $BaNb_2$, respectively.

The Ba-Sb, Sb-O, Zn-Sb, and Nb-Sb bonds are formed when Sb partially replaces Nb, and their lengths are also shown in Table 1.

| Bond name | Calculated (Å) | Formable structures |
|---|---|---|
| Ba-O | 3.165 | $Ba_2O_3$ |
| Nb-O | 2.289 | $Nb_2O_5$ |
| Zn-O | 2.243 | ZnO |
| Ba-Sb | 2.748 | $BaSb_2$ |
| Sb-O | 2.427 | $Sb_2O_5$ |
| Zn-Sb | 1.886 | ZnSb |
| Nb-Sb | 1.923 | $NbSb_2$ |

**Table 1.** Calculated Bond Length Values for a Potential Formable $Ba(Zn_{1/3}Nb_{2/3-x}Sb_x)O_3$ Ceramic (Qasrawi, Sahin, et al., 2019).

The probable formable compounds found inside the BZN's structure are indicated by the bond length listed.

The analysis of bond lengths in the studied material reveals that the Zn-Sb bond is the shortest, indicating a strong bond between these elements. Following this, the Nb-Sb bond is slightly longer. This observation suggests a preference for the formation of ZnSb and $NbSb_2$ compounds in addition to the other minor phases listed in Table 1.

The bond lengths provide insight into the bonding characteristics and the likelihood of specific compound formations within the material

Figure 25 (a) clearly shows that the perovskite structure of BZN consists of Ba atoms occupying the A sites (corners) and oxygen (O) atoms at the face-centered cubic sites. On the other hand, the B sites in the structure are occupied by elements such as Nb, Zn, or Sb, which have a pentavalent (five valence electrons) configuration.

Three elements Zn (which makes up one-third), Nb and Sb (which make up the other two-thirds), which occupy the latter center share the central location (Şahin,2010; Qasrawi, Sahin, et al., 2019).

## 11. SEM (JEOL JSM 5910LV) AND SEM COATING (Au/Pd) DEVICE (Polaron Range Sputter Coater-SC7620)

The scanning electron microscope (SEM, JEOL JSM 5910LV) is one of the versatile instruments widely used to show the topographic features, morphology and phase distribution on the sample surface (Figure 26).

SEM is one of the most versatile instruments used to demonstrate topographic characteristics, morphology, and phase distribution on the sample surface. It is a potent magnification tool (Sahin, 2010; Topcu & Ceylan, 2020).

The microstructures of the sintered samples were examined by scanning electron microscopy and the analysis of the phases formed in the inner structure was carried out using energy distribution spectrometry (EDS).

The following describes the primary working principle of SEM:

In a very high vacuum, a constant stream of electron beams is produced by the electron guns at the upper part of the column. These beams are then accelerated by using a high electric potential before being directed into the sample. Voltages of 2 to 50 kV are often used for SEM (Şahin, 2010; Şahin, 2019; Ibrahim, 2015).

A monochromatic beam is generated by controlling and directing the flow of particles or photons through magnetic lenses, which restricts the beam's spread, focuses it, and aligns it in a specific direction.

Upon interaction of the monochromatic electron beam with the sample, the sample emits signals that contain valuable information regarding surface topography and composition. These signals can be used to analyze and characterize the sample.

The signals are subsequently translated into images by a number of detectors.

SEM uses secondary electrons (SE) and backscattered electrons (BSE), two different categories of imaging techniques.

SEs are generated through inelastic scattering processes when the incident electrons lose energy and are ejected from the surface of the sample. On the other hand, BSEs are created through elastic scattering processes where the incident electrons are scattered back without losing much energy.

To avoid static charge accumulation on the sample if the sample is an insulator, it should be coated with a thin coating of gold or carbon (Ibrahim, 2015).

Thanks to the EDS on the SEM, information is obtained about the chemical composition of the material and information about the chemical formula of the material can be obtained by detecting the elements (%) in the material (Şahin, 2019; Şahin, 2010).

**Figure 26.** A Picture of the SEM (JEOL 5910-LV) Setup in the Testing Room for the Material with EDS (Oxford-Inca-7274) (Sahin, 2019; Sahin, 2010)

In modern systems, the signals from these sensors are converted into digital signals and transmitted to a computer monitor for visualization and analysis.

The discrimination power of some scanning electron microscopes can be as low as 0.05 nm (Şahin, 2010).

In the SEM device, a beam of electrons with high energy is sent to the sample and the incoming electron beam is scattered from the surface.

So that the atoms of the sample can be seen microscopically, and we also obtain topographic information about the surface of the sample.

The sintered samples were first adhered to the aluminum sample holder using carbon tape and then coated with a gold/palladium alloy for surface conductivity in SEM analysis.

The fracture surfaces of the samples are analyzed using a scanning electron microscope (SEM) operating at 20 kV. Prior to imaging, the samples are coated with an Au/Pd alloy using a sputter coater. (Figure 26).

The coating process was carried out with a Polaron Range Sputter SC7620 model coating device by giving a current of 4 mA in an average of 3 minutes (Figure 27).

**Figure 27.** SEM Coating (Au/Pd) Device (Polaron Range Sputter Coater-SC7620) (Sahin, 2019; Sahin 2010)

Microstructure analyses of the samples were performed using Low Vacuum Scanning Electron Microscopy (SEM, JEOL 5910-LV) and Energy Dispersion Spectrometer (EDS, Oxford-Inca-7274) (Figure 26).

The scanning electron microscope here operates at 20 KV, and the surfaces and fracture surfaces of the samples are examined using secondary electron imaging (SEI) and backscattered electron imaging (BEI) techniques.

While SEM was used to identify the phases and examine the microstructure in the study, chemical analysis was performed using energy dispersive spectrometry (EDS).

The nickel contribution to the $Ba(Zn_{1/3}Nb_{2/3})O_3$ (BZN) ceramic structure was employed in accordance with the empirical formula $Ba(Zn_{1/3-x}Ni_xNb_{2/3})O_3$ in the SEM measurement investigation we conducted, which is presented below (Şahin, 2010; Qasrawi, Şahin & Emek, 2021).

Figure 28a shows an example of a 2000-fold enlargement of a scanning electron microscope picture of $Ba(Zn_{1/3-x}Ni_xNb_{2/3})O_3$ ceramics.

The picture shows very condensed grain dispersion.

For this sample, the average grain size is close to 1.1 μm.

The nature of construction is attributed to the significant difference between the size of the grains and the size of the crystallites as determined by x-ray diffraction.

In other words, several crystallites can be found inside a single grain (Sahin, 2010; Sahin, 2019; Qasrawi, Sahin, et al., 2019); Qasrawi, Sahin and Emek, 2021; Qasrawi, Sahin, et al., 2021).

The XRD method is more suitable for estimating the crystallite size rather than the grain size because X-rays interact with the atoms within the crystalline structure and undergo diffraction, providing information about the arrangement of atoms and the crystal lattice.

Multiple locations were selected to determine the composition of BZN. One of these locations, indicated by a pink-colored rectangular shape, was specifically analyzed for its BZN composition.

Based on the energy dispersive X-ray (EDS) compositional studies shown in Figure 28c, the composition of BZN consists of Ba, Zn, Nb, Ni, and O with weight percentages of 48.27%, 6.36%, 24.82%, 0.60%, and 19.95%, respectively.

The scanning electron microscope (SEM) images revealed that the increase in Ni content in the BZN did not have a significant impact on the grain size or the overall surface morphology.

These figures guarantee Ni's solubility in the BZN ceramics.

However, at a magnification of 5000 times (as shown in Figure 28b), small grains that are rarely observed (indicated by blue circles) were found near the grain boundaries (Qasrawi, Sahin and Emek, 2021).

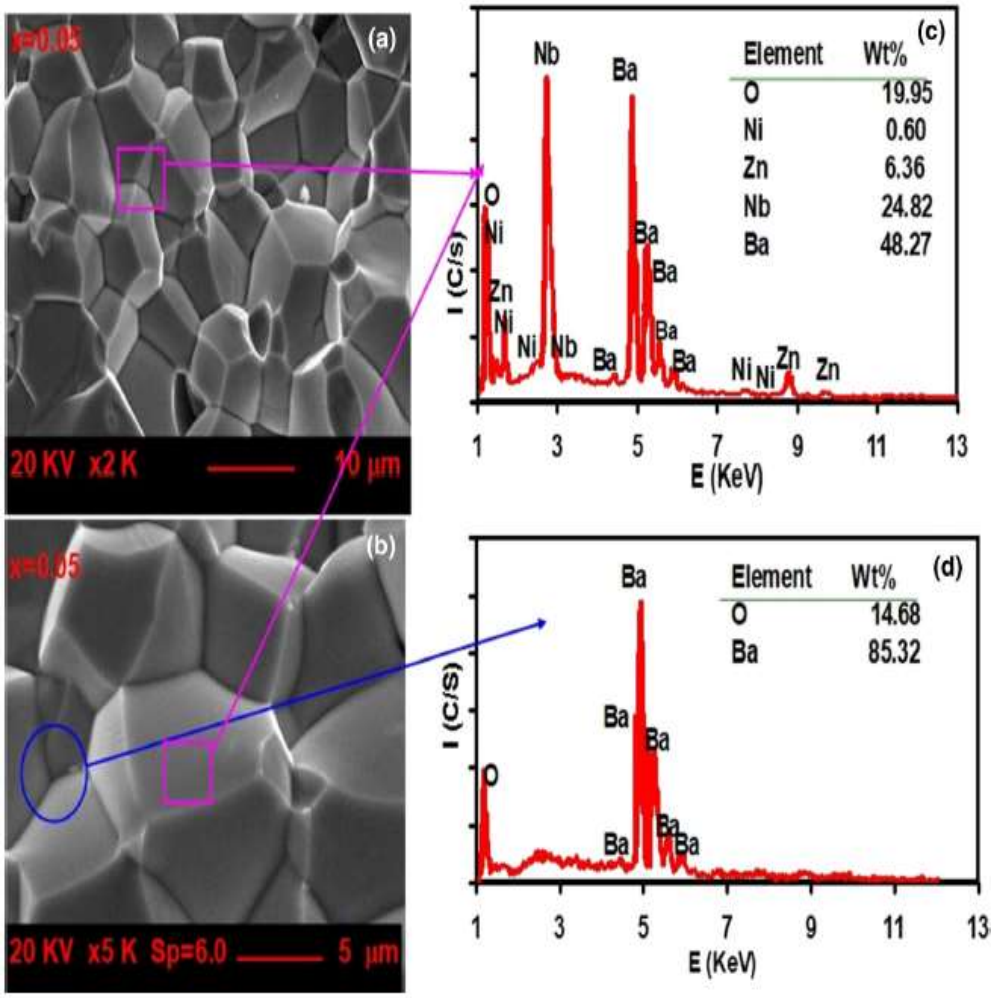


**Figure 28.** The Photos from Scanning Electron Microscopy as an Illustration of Ni-doped $Ba(Zn_{1/3}Nb_{2/3})O_3$ Ceramics with x = 0.05 Ni Concentrations. a) 2000x Enlargement, b) a 5000x Enlargement Demonstrating the Presence of Minor Phases in the Samples, c) an Energy Dispersive x-ray (EDS) Examination of the Big Grains (major phase), and d ) an EDS Analysis of the Minor Phase ($Ba_2O_3$) (Qasrawi, Sahin and Emek, 2021).

The spectra in Fig. 28d show the results of the EDS test for these locations, which show that the grains are 85.32 weight percent Ba and 14.68 weight percent O.

Through XRD analysis, the minor $Ba_2O_3$ phase was also identified, and it was found that in these samples, when the Ni concentration is x = 0.05, it has a phase weight of 1.06%.

The SEM images provided additional evidence that increasing the Ni concentration in BZN does not impact the grain size or the overall surface morphology.

SEM samples were examined in a different study below.

SEM analysis was done on specimens that were sintered at 1100 °C for 4 hours. In all samples, $ZnNb_2O_6$ single-phase structure was created, according to SEM examination (Figures 29 a and b). No additional phase or impurity was detected in the microstructure (Sahin, 2022).

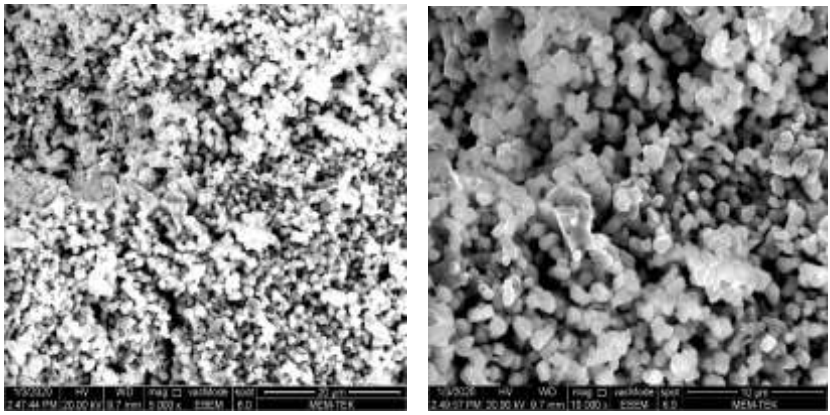

a b

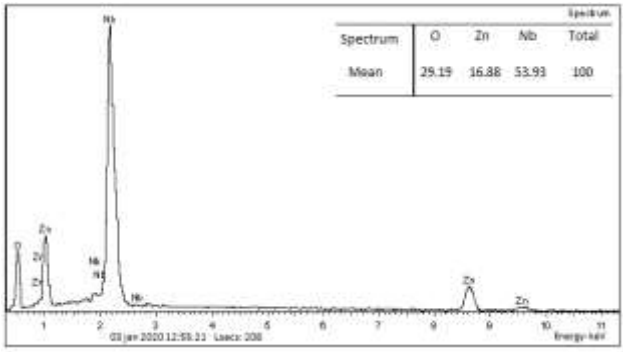


c

**Figure 29.** SEM Pictures of Single-phase $ZnNb_2O_6$ sintered for 4 h at 1100 °C a) at x 5000, b) at x 10000, c) EDS Analysis of the Material at x 5000 (Sahin, 2022)

It was understood that the microstructure created grains with complementary morphologies.

The majority of grains are spherical, and the EDS analysis found no discernible compositional differences between grains with various morphologies.

The $ZnNb_2O_6$ grains' EDS analysis findings showed values that were very similar to the predicted $ZnNb_2O_6$ composition (16.8% Zn, 53.9% Nb, and 29.1% O) (Şahin, 2022).

The grain size appears to be consistent when the particle size is evaluated at different magnifications. (Figure 29 c).

## 12. TWO PORT VECTOR NETWORK ANALYZER (VNA) (R&S FSH-K 42) and NETWORK ANALYZER DEVICE (N 5230A PNA Series- AGILENT TECHNOLOGIES)

### 12.1 Two Port Vector Network Analyzer (VNA) (R&S FSH-K 42)

Shielding efficiency and reflection loss measurements are performed via a two-port VNA (R & S FSH-K 42) equipment (Figure 30).

The microwave shielding efficacy or reflection loss values of composite or various materials may be calculated using a two-port VNA (R & S FSH-K 42) equipment operating at a wideband frequency (0-8 GHz), including L, S, and C radar frequency bands.

The VNA device used for the measurements is equipped with N-type inputs and is capable of conducting two-port cable-type measurements. The tests were conducted using a coaxial holder with suitable diameters to ensure a 50 Ohm impedance at the input and output ports (Şahin, 2019; Şahin, 2023).

In order to perform SE or RL tests, it is essential to use coaxial holders with appropriate diameters that ensure a 50-ohm impedance at the input and output ports.

Firstly, a non-sample value is calculated as a blank. In order to maintain consistent pressure throughout the sample, samples are then sequentially inserted in the instrument and evenly squeezed at three separate places at all times (Sahin, Emek, et al., 2023).

The device sends the output data to a computer for the evaluation of electromagnetic interference shielding effectiveness (EMI-SE) values and reflection loss (RL) of the sample samples.

The computer displays the difference between the presence and absence of samples as shielding efficiency or reflection loss values, depending on the desired measurement result shown on the device's screen.

By repeatedly measuring the smooth round samples of a specific thickness, the device's measurement is verified.

For example, when the shielding effectiveness is -20 dB, it indicates that the incoming electromagnetic wave is attenuated by 99 percent and only 1 percent of it is transmitted through (Sahin, 2019; Sahin, 2022; Sahin, 2023; Chung, 2000; Ting, Yu and Jau, 2011).

Similar to the last example, we know that at 30 dB there is a 99.9% drop and a 0.01 percent crossing over (Şahin, 2019; Chung, 2000).

The measured electromagnetic interference shielding effectiveness (EMI-SE) and reflection loss (RL) values of the composites are correlated with the geometry and orientation of the samples, with sample thickness being a crucial parameter, preferably thin (Şahin, 2022; Şahin, 2023; Yang, Lozano, et al., 2005).

**Figure 30.** R&S@FSH-K 42 Spectrum Analyzer (Şahin, 2019),(www.rohdeschwarz.com, www.testequipmenthq.com)

The blank sample area and load sample must be about the same in thickness for the greatest repeatability of SE or RL measurements.

The amount of shielding effectiveness is determined by how much of the incoming electromagnetic wave passes across the composite material.

If the EMI cannot travel through, it will be reflected or absorbed by the substance.

In other words, separate measurements are necessary with this device since the material that provides the EMI shielding effect function either has a back reflection or absorption.

In the sample measurement below, the SE measurement results of the polymer-based doped BZN composite are included.

In terms of microwave shielding efficacy, this research investigated for the first time the possible application of composites consisting of polyaniline (PANI) and copper-doped nickel ferrite ($NiFe_2O_4$) (Şahin, 2019; Şahin, Emek, et al., 2023).

The findings demonstrate that the epoxy-(PANI/$NiFe_2O_4$:Cu) composites have various SE properties depending on their composition.

As compared to epoxy-$NiFe_2O_4$:Cu composites/Aniline: 1/1, the epoxy-$NiFe_2O_4$:Cu composites/Aniline: 1/3 had a more noticeable influence on the shielding effect features.

In Figure 31, the conclusions of a study on the electromagnetic shielding efficiency of several composites are displayed.

The results are as follows:

Because of their easy and cost-effective manufacturing techniques, PANI/Cu-added nickel ferrite composites have the possibility to be used as efficient microwave shielding materials.

The lowest shielding efficacy point for epoxy-PANI/$NiFe_2O_4$:Cu compositions shifted toward higher frequencies as PANI concentration rose.

The $NiFe_{1.7}Cu_{0.3}O_{3.85}$/Aniline: 1/3 composite demonstrated microwave shielding efficiency at a frequency of 6.82 GHz and a thickness of 2.0 mm, with the lowest SE of 29.74 dB.

At high doping concentrations, the ability of copper-infused $NiFe_2O_4$ to screen microwaves varies significantly.

$NiFe_{1.7}Cu_{0.3}O_{3.85}$/Aniline: 1/3 compositions, on the other hand, exhibits shielding effectiveness of less than -20 dB in the frequency ranges of 5.32-6.69 GHz and 6.79-7.4 GHz, respectively.

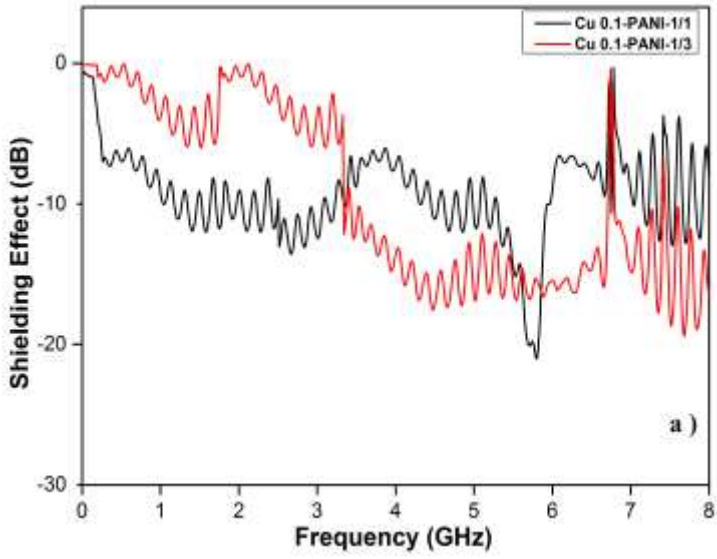
Cu 0.1-PANI-1/1
Cu 0.1-PANI-1/3
Shielding Effect (dB)
Frequency (GHz)
a )

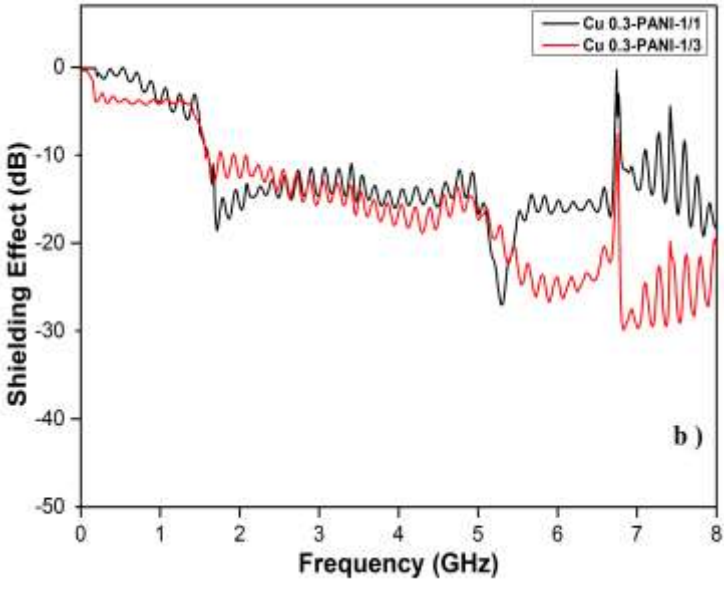
Cu 0.3-PANI-1/1
Cu 0.3-PANI-1/3
Shielding Effect (dB)
Frequency (GHz)
b )

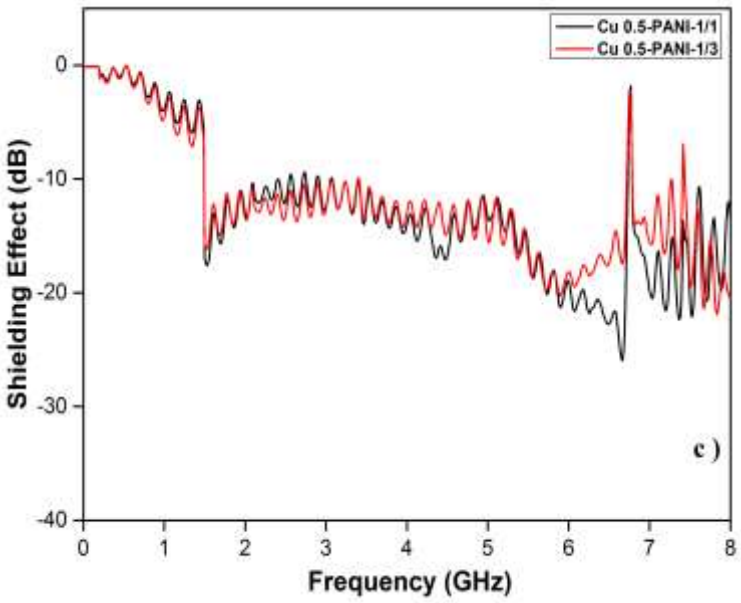


**Figure 31.** Shielding Properties of the Epoxy-(polyaniline/$NiFe_{2-x}Cu_xO_4$) composites a) x=0.1, Cu doped Ni Ferrite/ Aniline Ratio was changed as 1/1, 1/3 b) x=0.3, Cu doped Ni Ferrite/ Aniline Ratio was changed as 1/1, 1/3 c) x=0.5, Cu doped Ni Ferrite/ Aniline Weight Ratio was altered as 1/1, 1/3 (Şahin, 2019; Şahin, Emek et al., 2023)

It is possible to test the absorbance and shielding effectiveness of PANI-single phase Cu-doped $NiFe_2O_4$ with different dopants in various radar and higher frequency bands.

These tests can provide valuable information about the material's performance in terms of absorption and electromagnetic shielding in specific frequency ranges (Şahin, Emek, et al., 2023).

The findings, which are consistent with previous studies (as shown in Table 2), have important implications for the development of new composite materials with improved electromagnetic shielding properties (Şahin, Emek et al., 2023).

These materials can find diverse applications where effective electromagnetic shielding is required.

| Sample | SE dB | Frequency GHz |
|---|---|---|
| $NiFe_{1.9}Cu_{0.1}O_{3.95}$/Aniline: 1/1 | −21.05 | 5.8 |
| | −20 | 5.76–5.82 |
| | −10 | 2.53–2.9, 5.32–5.91 |
| $NiFe_{1.9}Cu_{0.1}O_{3.95}$/Aniline: 1/3 | −19.44 | 7.67 |
| | −10 | 3.43–6.71, 6.79–7.39 |
| $NiFe_{1.7}Cu_{0.3}O_{3.85}$/Aniline: 1/1 | −27.14 | 5.29 |
| | −20 | 5.14–5.46 |
| | −10 | 1.62–6.72, 7.63–8 |
| $NiFe_{1.7}Cu_{0.3}O_{3.85}$/Aniline: 1/3 | −29.74 | 6.82 |
| | −20 | 5.32–6.69, 6.79–7.4 |
| | −10 | 2.11–6.73, 6.77–8 |
| $NiFe_{1.5}Cu_{0.5}O_{3.75}$ /Aniline: 1/1 | −26.02 | 6.67 |
| | −17.55 | 1.53 |
| | −10 | 1.48 to 2.54, 3.08 to 6.72, 6.8 to 8 |
| $NiFe_{1.5}Cu_{0.5}O_{3.75}$ /Aniline: 1/3 | −21.89 | 7.84 |
| | −10 | 1.48 to 3.37, 3.41 to 6.72, 6.79 to 7.4, 7.44 to 8 |

**Table 2.** The Shielding Performance in GHz of Epoxy-(Polyaniline/ $NiFe_{2-x}Cu_xO_4$) Composites with the Ranges of Shielding.

## 12.2 Network Analyzer Device (N 5230A PNA series- Agilent Technologies)

The Agilent Technologies N 5230A PNA series Network Analyzer was used for the SE measurements (Figure 32), (Şahin, 2019; Şahin, 22).

Coaxial holders with appropriate diameters were used for SE testing to ensure a consistent 50-ohm impedance at the input and output ports.

A value without a sample was initially calculated as a baseline.

The samples were sequentially inserted into the device, with consistent pressure applied by uniformly pinching them from three different locations.

The device sends the output values to the computer, which computes SE.

The shielding efficacy values were displayed on the computer as the difference between the presence and absence of the samples.

This flanged coaxial EMI SE tester is a flanged coaxial tester with constant diameters and a 50 ohm impedance over its whole length.

The specimen holder is a long coaxial transmission line with specifically engineered taper sections and matching notches to maintain a constant 50 ohm characteristic impedance along its length (Yang, Lozano, et al., 2005; Uçar, Kavaoğlu, et al., 2018).

**Figure 32.** N 5230A PNA Series Network Analyzer (Agilent Technologies) (Şahin, 2019; Şahin, 2022)

In Figure 33 below, an image of the same device is given during the experiment.


**Figure 33.** N 5230A PNA Series Network Analyzer Device Image During the Experiment (Agilent Technologies) (Şahin, 2019)

To verify the device's measurement, specimens with a smooth, 1.5 mm-thick, and rectangular shape were regularly measured.

Composites' recorded SE values depend on geometry and orientation; therefore, for the highest reproducibility of SE measurements, the reference specimen space and load specimen have to have the same thickness.

In the example below, the SE measurements of the composite formed by combining $ZnNb_2O_6$ structure and chopped strands in certain proportions are given (Şahin, 2022).

Composites can eliminate the desired deficiencies of the new material (Topcu, 2020).

The frequency dependence of the shielding effectiveness of the epoxy-chopped strands/$ZnNb_2O_6$ composites is shown in Figure 34 for the frequency range of 6.5–18 GHz (Şahin, 2022).

The microwave shielding properties of the $ZnNb_2O_6$ / chopped strands composites were clearly better than those of $ZnNb_2O_6$ -chopped strands (at 60-40 wt%) than those of $ZnNb_2O_6$ -chopped strands (at 80-20 wt%).

In $ZnNb_2O_6$ -chopped strand compositions (at 60-40 wt.%), there was only one band at 6.72 GHz with -51.32 dB.

At 11.02 GHz and 16.55 GHz, respectively, this composite material has a -34.47 dB and -36.25 dB.

The compositions also exhibited shielding effectiveness of less than -20 dB in the frequency ranges of 6.5 GHz and 6.84 GHz, 7.86 GHz and 15.17 GHz, 17.54 GHz and 17.88 GHz.

The $ZnNb_2O_6$ composite material (at 80-20 wt%) demonstrated a shielding efficiency of less than -20 dB in the frequency bands between 9.19 GHz and 11.72 GHz, 16.65 GHz, and 16.93 GHz as the quantity of zinc niobate powder increased and the proportion of chopped strands decreased.

The best broadband shielding was provided by the chopped strands/$ZnNb_2O_6$ (at 60-40 wt%), which had a value of less than -20 dB between 7.86 GHz and 15.17 GHz (Şahin, 2022).

Chopped strands were employed to improve the corresponding impedance of the composites' components during transmission.

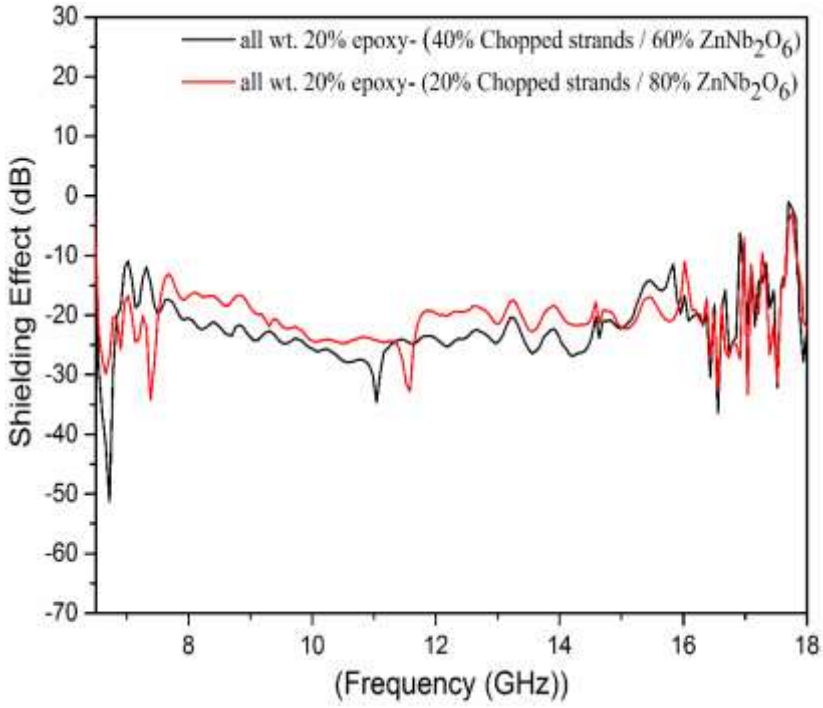


**Figure 34.** Shielding effectiveness of the epoxy-(chopped strands/$ZnNb_2O_6$) composites: all wt. 20% epoxy- (40% chopped strands / 60% $ZnNb_2O_6$), all wt. 20% epoxy- (20% chopped strands/ 80% $ZnNb_2O_6$) (Şahin, 2022)

The distinct peaks in the shielding effect are attributed to the resonance effect resulting from the geometry of the holder and the reflection of electromagnetic waves.

The shielding effectiveness (SE) test is used to calculate the amount of insertion loss induced by sandwiching a material between the source and the signal analyzer. (Şahin, 2022; Şahin, Emek et al., 2020; Şahin, Cantürk et al., 2021; Şahin, Emek and Ibrahim, 2022, Şahin, 2023; Şahin, 2022).

Reflection loss, determined by the interaction of mobile charge carriers with electromagnetic (EM) waves, is a factor influencing electromagnetic interference (EMI) shielding. Another factor is absorption loss, which is influenced by the interaction of magnetic and electrical dipoles with EM waves.

The multiple reflection effect, also known as the third mechanism, refers to internal reflections occurring within the shielding material. It is another factor influencing electromagnetic interference (EMI) shielding.

Internal reflections in the shielding material cause the multiple reflection effect, which has an influence on EMI shielding. This impact is accentuated by the presence of multiple large surface areas or interfacial regions in the material (Şahin, 2022; Şahin, 2023, Shukla, 2020; Şahin & Emek, 2023).

## 12.3 Reflection Loss (RL) Measurements

The rapid expansion of the communications industry has generated significant interest in microwave-absorbing materials.

With the recent transition of contemporary communication systems to higher frequencies, there has been a natural increase in interest and demand for absorber materials that can operate at these frequencies. (Şahin, 2019, Şahin 2022).

To effectively absorb the signal, it is necessary for the absorber material to prevent reflection in the direction it came from and minimize transmission. This requires the signal to be absorbed within or on the material itself.

Normally, when the reflection coefficient reaches the minimum level, the lowest reflection loss is obtained; that is, none of the incoming electromagnetic waves are reflected back (Şahin, 2019).

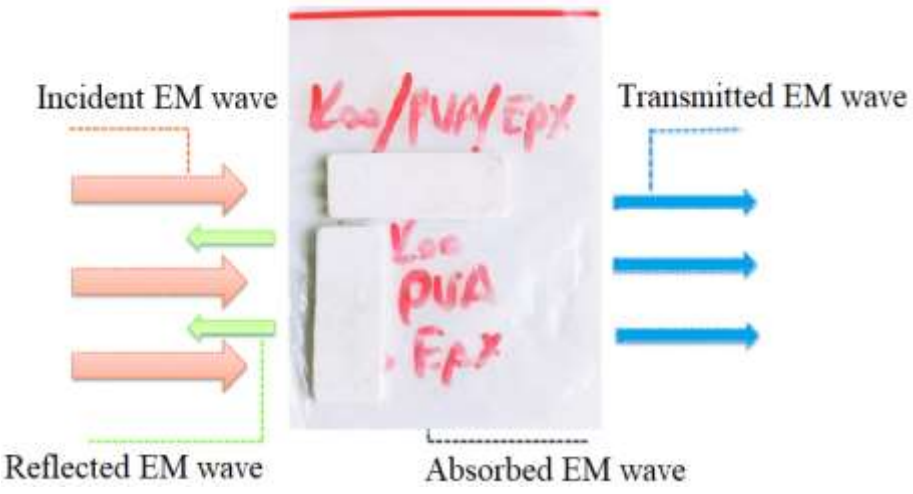


**Figure 35.** The Incident Electromagnetic Wave's Schematic

The primary purpose of an electromagnetic absorber coating is to minimize reflection and maximize the absorption of incoming electromagnetic waves.

This ensures that the waves are effectively absorbed by the coating rather than being reflected back.

It also includes reflected microwave surface reflection and multiple reflections, as shown, for example, in Figure 35.

The Kaolinite/PVA composite in Figure 35 is a trial sample used for the n 5230A PNA series network analyzer; the SE values of this sample were determined in a separate study (Şahin & Emek, 2023).

To achieve effective absorption, it is necessary to minimize reflection at the material surface and promote multiple reflections within the material. (Sun, He et al., 2013).

The value of electromagnetic wave absorber materials is related to how thin a layer and how wide a frequency range it absorbs (Şahin, 2019).

RL values were determined in the study below for RGO/P- $Fe_3O_4$/PANI composite (Lin, Yu ve et al., 2021) (Figure 36).

As more electromagnetic waves penetrate inside the absorbing material, there will be greater opportunities to achieve lower reflection loss (RL) values, typically below -10 dB. This is because a higher degree of wave penetration allows for increased absorption within the material, reducing the amount of reflected energy. (Liu, Huang et al., 2013).

As a result of the porous $Fe_3O_4$ nanosphere, the composite provided increased chances for multiple reflection loss.

Because both magnetic and dielectric materials were added, good impedance matching was also demonstrated.

The saturation magnetization and the ferromagnetic behavior could both be reduced by lowering the $Fe_3O_4$ concentration, while the coercivity performance exhibited the reverse trend and exhibited a larger magnetic hysteresis loss.

According to the comments of the researchers;

Porous $Fe_3O_4$ nanospheres were added to the RGO (reduced graphene oxide) surface in this study, increasing the interface and heterogeneous area, which allowed space charge to build up and result in better microwave absorption properties.

A substantial polarization in the PANI chain was also facilitated by the dipolar found on the surface of the conjugated polymers of PANI.

In this study, The PANI/RGO/$Fe_3O_4$ ternary composite was shown to be a potential candidate for a microwave absorber when the minimum RL value was measured at -29.51 dB with a thickness of 1.0 mm. (Luo, Xu et al., 2015; in, Yu et al., 2021).

In another study in the literature, researchers made the following comment according to the measurement results for FeSiCr@$Fe_2O_3$ nanoparticles made with the Network analyzer device (Wang et al., 2021).

1.5 g of created FeSiCr nanoparticles were then placed in a resistance furnace with a high vacuum and high temperature.

The nanoparticles were oxidized and heated at a certain temperature (100, 125, 150, or 200 $^oC$). 0.1 MPa dry air environment, a 30-minute holding period, and a 5 $^oC$/min heating rate were used (Wang et al., 2021).

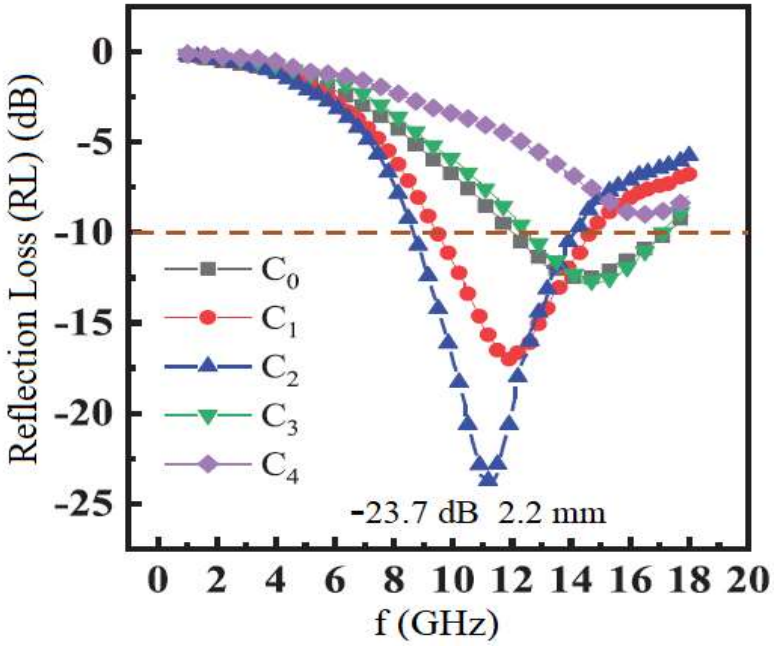


**Figure 36.** The Reflection Loss of the Specimens $C_0$, $C_1$, $C_2$, $C_3$ and $C_4$ (Wang et al., 2021)

150 $^o$, 175 $^o$ and 200 $^o$ Celsius correspondingly were the vacuum heat treatment temperatures. Samples that have undergone oxidation heat treatment are designated $C_1$, $C_2$, $C_3$, and $C_4$, whereas the initial samples that did not undergo this treatment are designated $C_0$ in this experiment.

Figure 36 displays the RL curves for $C_0$, $C_1$, $C_2$, $C_3$, and $C_4$ in the frequency range of 2-18 GHz (Wang et al., 2021).

Figure 36 demonstrates that among the samples $C_0$-$C_4$, $C_2$ has the lowest reflection loss, exhibiting the highest absorption ability.

$C_2$ has a minimum reflection loss (RL min) of 23.7 dB at 11.2 GHz (d = 2.2 mm), and its effective absorption bandwidth (RL 10 dB) is 5.6 GHz (Wang et al., 2021).

In another study, measurements were made similar to the SE and RL measurements, and the researchers designed a frequency-selective material. As a different geometry, "Three-legged loaded" loop-type element geometry was chosen (Kartal, Pinar, et al., 2013).

In another study, the researchers developed a compound using a Field Coated Grading Honeycomb (ACGH) structure and a frequency selective surface (FSS) in a distinct study described in the literature (He, Si et al., 2022).

The images of the prototypes made, as well as the measuring equipment, are shown in the image below (Figure 37).

The reflectivity of the fabricated FSS absorber materials was analyzed using a vector network analyzer within the frequency range of 1-18 GHz.

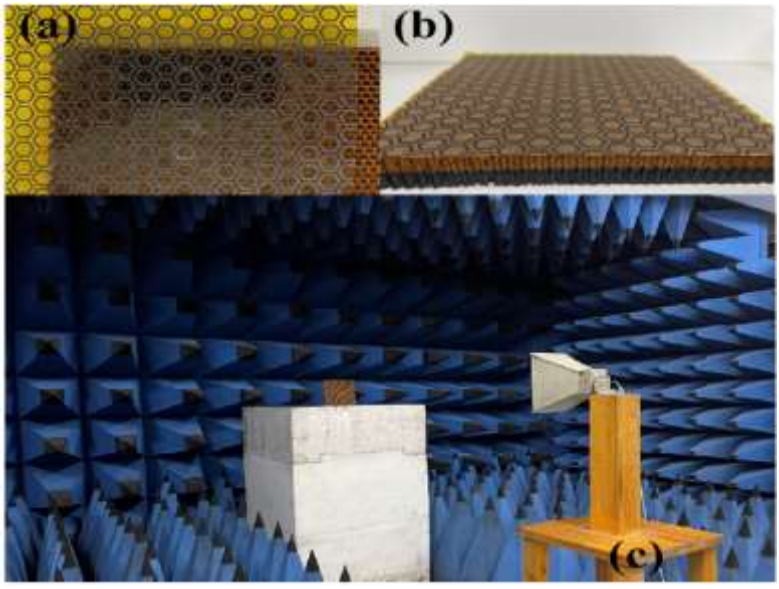


**Figure 37.** Pictures of the Manufactured Prototypes and the Measuring Apparatus a) An FSS Absorber with a 7 mm Thickness b) A 17 mm Thick ACGH-FSS Absorber c) A Free-space Measuring System (He, Si et al., 2022)

The following conclusions were reached in other studies for SE and RL measurements;

It is necessary that the signal coming to the absorber material should not be reflected in the direction it came from and should not provide transmission at the same time.

For this, the signal must absorb in or on the material.

Normally, when the reflection coefficient reaches the minimum level, the lowest reflection loss is obtained; that is, none of the incoming electromagnetic waves are reflected back.

In principle, the role of an electromagnetic absorber coating is to provide low reflection and high absorption for incoming electromagnetic waves.

The shielding efficiency and reflection loss properties of the materials to be produced for these devices can be improved by using various additives and different types of polymers (Şahin, 2019).

They can also be investigated by making composite materials, and measurements can be taken by producing triple composites by adding boron-derived minerals to polymer-based doped nickel ferrites (Şahin, 2019).

## 13. ION CHROMATOGRAPHY (IC) DEVICE (940 Professional IC Vario)

Ion chromatography (Figure 38) can detect anions and cations in different aqueous solutions down to the one billionth concentration.

Utilizing ion exchange resins, ion chromatography is a technique for separating and analyzing ions. Both cation exchange resins and anion exchange resins are used to separate anions and cations, respectively.

Based on how the ions interact with the resin (stationary phase) and eluent (mobile phase), ion chromatography is a technique for separating the ions.

These phases are different between an anion column, which draws anions, and a cation column, which draws cations. Only the conductivity of the particular sort of ion that each column attracts may be measured.

Ions will pass through the ion chromatographer's columns at various speeds depending on their affinity for the particular resin, and they will segregate from one another based on variations in ion charge and size.

Ions that have a lesser affinity for the resin will go through the column more quickly and be eluted first when the eluent passes through it, whereas ions

that have a greater affinity for the column would move through it more slowly (Yılmaz, 2013; Uçar, 2011).

After leaving the column, the ions are measured by the electrical conductivity detector. The conductivity versus time is shown as a chromatogram by this specific detector (Harris, 2007).

Ion chromatography is frequently used for the following purposes:

Rainwater analysis, checking drinking water for contaminants, assessment of wastewater's constituents, determination of water chemistry in an aquatic ecosystem, determination of sugar and salt content in food products, and isolation of selected proteins.

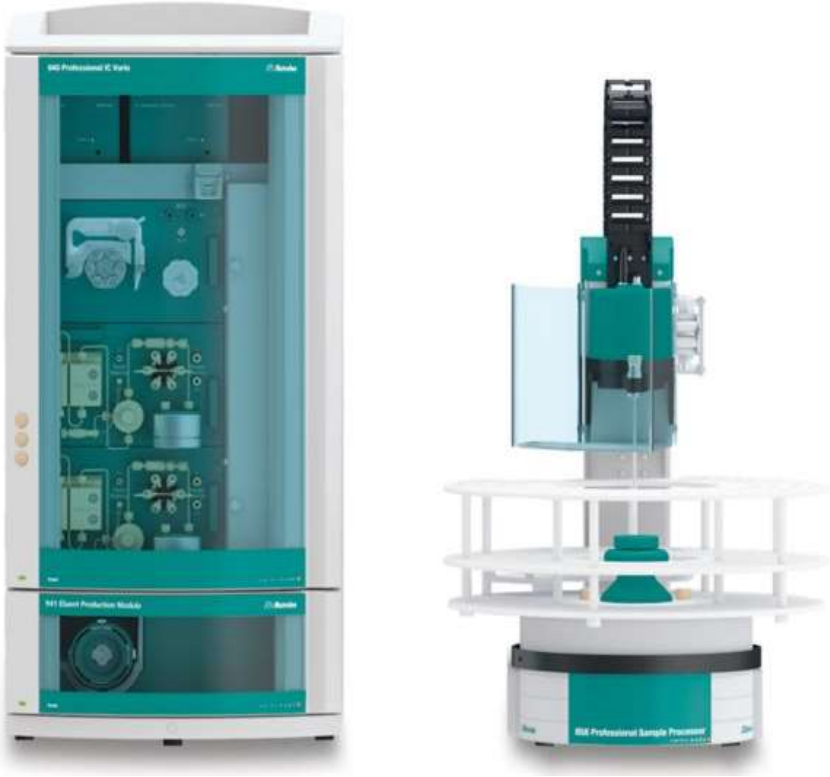

**Figure 38.** Ion Chromatography (IC) Device (Metrohm, 940 Professional IC Vario),(www.metrohm.com,www.metrohm.com/tr_tr/products/ionchromatography/940-professional-ic-vario.html)

There are important studies in the literature on this device. For example, in a study, perchlorate analysis was performed in various samples using ion chromatography (Uçar, 2011).

The evaluations made highlighted the following:

Perchlorate exposure, neural brain damage, and skeletal damage are all potential risks for fetuses and newborns.

Since the thyroid glands, where perchlorate is found, are crucial for brain development, milk is recognized to be crucial for human health, particularly for infants and young children.

Perchlorate was identified in milk samples in this investigation in measurable amounts.

The feed and water supplies used to hydrate the cattle are the major sources of perchlorate.

Turkey's water samples were examined to determine the level of perchlorate contamination using a variety of water samples (pool, tap, and surface water).

Perchlorate contamination was not found in large quantities in the water samples, according to the research (Uçar, 2011).

In a different study in the literature, the following conclusions were reached.

In the study, the geothermal energy potential of Aydın was emphasized and the analysis of the hot spring waters in this region was made (Yılmaz, 2013).

The temperature data were greater than the average data from the nearby provinces' hot springs.

The conclusion is that Aydn thermal springs are appropriate for both thermal tourism and heating needs.

Numerous anions (F, Cl, Br, I, $NO_3$, $NO_2$, $SO_4$, $PO_4$), cations (Na, K, Ca, Mg, $NH_4$, Mn, Fe), and trace elements (Cd, Cr, Ni, Pb, Ba, Cu, Zn, Al, etc.) were analyzed in this work.

It was found that the amounts of heavy metals in the examined hot spring waters were below the thresholds that pose a risk to the general public's health (Yılmaz, 2013).

## 14. GC/MS (GAS CHROMATOGRAPHY/MASS SPECTROMETER ) DEVICE (7000E Triple Quadrupole)

The combination of two potent analytical methods is known as gas chromatography/mass spectroscopy (GC-MS) (Figure 39).

As known, a GC/MS device performs structural analysis and quantification by combining GC (Gas Chromatography) and MS (Mass Spectrometer) components.

In other words, gas chromatography-mass spectrometry (GC-MS) is an analytical method that combines the separation capabilities of gas chromatography with the identification and quantification capabilities of mass spectrometry. It is utilized to analyze and identify various compounds in a sample (Fang, Ivanisevic et al., 2015; Jones, 2019; Sparkman, Penton and Kitson, 2011).

The components in the mixture are separated using gas chromatography. The structural identification of each component is aided by mass spectrometry.

The device identifies components at the molecular level. Liquid, solid, and gas samples can all be used in GC-MS analysis (Jones, 2019).

The components of the GC-MS device include the GC intake, interface, ion source, mass analyzer, detector, and vacuum system. With ppm (one in a million) and ppb (one in a billion) sensitivity, GC-MS device can analyze all types of chemicals containing volatile organic molecules.

Classifying volatile and semi-volatile substances is the major function of the device. In GC/MS combinations, MS acts as a detector (Fang, Ivanisevic, et al., 2015; Jones, 2019; Sparkman, Penton and Kitson, 2011).

A qualitative determination may be accomplished by deriving the mass spectrum of each molecule from the chromatograms of the compounds supplied from the GC to the mass spectrometer.

It has major features such as being rapid, great separation power, capacity to do qualitative-quantitative analysis and high sensitivity.

The most common application areas of this device are:

Oil analysis, analysis of aromatic compounds, volatile or semi-volatile substances, qualitative and quantitative analysis of petroleum products, forensic medicine and drug analysis, analysis in sectors such as pharmaceutical, environment, chemistry, petroleum derivatives and petrochemicals (Jones, 2019; Sparkman, Penton and Kitson, 2011).

It has applications in various industries, including the analysis of food samples, oil samples, cosmetic products, and the determination of doping substances. The high sensitivity and selectivity of GC-MS make it a valuable tool for identifying and quantifying compounds in complex samples (Aksakal, 2016; Mert & Aras, 2022, Kıvrak, 2013).

**Figure 39.** GC/MS Device (7000e Triple Quadrupole-Agilent) (Agilent Technologies) (www.agilent.com)

Research with this device measured the levels of volatile organic chemicals that kids and staff at schools are exposed to and which are considered to have an impact on human health.

Gas chromatography-mass spectrometry (GC/MS) was used to measure the samples that were obtained within the scope of the study. Passive in 10 schools determined around the city of Iğdır for measurement, the air sampling device was left for a total of 12 days.

According to the findings, toluene (6.8 µppm), acetone (5.4 µppm) and ethanol (39.5 µppm) values are different according to the coordinates of the schools and these values were found to be high compared to other compounds (Mert & Aras, 2022).

These values, it has been determined, are within acceptable reference ranges.

In another study, biomonitoring of natural mycotoxin zearalenone and its metabolites in cereal-based baby foods was performed with this device. In this study, commercially available cereal-containing infant formulas were examined for the existence of Zearalenone and its metabolites (α-ZOL and β-ZOL) (Aksakal, 2016).

The SPE method was employed for the analysis, the method's validation tests were carried out by enhancing the prior research in various phases, and the method was adapted for GC/MS.

No positive result that might indicate contamination in terms of ZON and its metabolites was found after analysis of 44 cereal-based infant foods.

In a further study, organochlorine pesticide residues were examined in mineral waters in the aybaş area, which is connected to the Osmangazi district of Bursa province and where there is a high level of mineral water production. Water resources are significantly harmed by pesticides, especially those used on agricultural land (Bal, 2021).

The first significant class of synthetic organic pesticides in the persistent organic pollutants family are organochlorine pesticides.

Chronic illnesses, bioaccumulation, and severe toxicity are further potential outcomes. On a GC-MS instrument, solid phase extraction (SPE) was used to conduct pesticide analyses.

19 distinct organochlorine pesticide residues from the samples obtained were investigated.

The investigation revealed that there were no traces of organochlorine pesticides found in the mineral water samples obtained from four different source locations and the final product. (Bal, 2021).

## 15. CONCLUSION

In this book, various measurement techniques for many materials are explained with experiments, and the characterizations of the materials are determined with different devices.

For material characterizations in this book, XRD, SEM, SEM coating device, XPS, FTIR, TG-DTA, two-port vector network analyzer (VNA), network analyzer (NA), IRMS, inverted microscopes, MP imaging device, dielectric measuring device, VSM, GC/MS and Ion chromatography (IC) have been explained with examples depending on the method and type of material.

Today, the source of most of the products we use in many sectors is the use of these laboratory devices and the measurement results.

The first stage of the material passes through these technical devices.

In addition, the benefits of the measuring device used are stated with examples and information about the advantages of usage in different areas.

With the developing technology, material characterizations have become increasingly important for many fields.

It is very important to characterize the physical, optical, chemical, morphological and mechanical characteristics of the produced materials. In fact, by focusing on controlling the microstructure of materials, we could reach the material with the intended properties or the parameters we want to find.

New technologies and the developments brought by these technological devices should be constantly followed.

Thanks to the characterization results, advances and innovations continue in the area of technology, health and engineering.

Future research and new inventions will result from the characterization of diverse materials and composites that are discovered.

## REFERENCES

Aksakal, T. B. (2016). *Tahıl Bazlı Bebek Mamalarında Doğal Mikotoksin Zearalenone ve Metabolitlerin Biyoizlenmesi*, Doktora Tezi, Gazi Üniversitesi Sağlık Bilimleri Enstitüsü, Ankara-Türkiye.

Arshad, M., Azam, A., Ahmed, A.S., Mollah, S., Naqvi, A.H.(2011). Effect of Co substitution on the structural and optical properties of ZnO nanoparticles synthesized by sol–gel route. *Journal of Alloys and Compounds*, 509 (33), 8378-8381.

Ayanoğlu, Z. G. (2019). *Metakrilat Türevi Polimerleri/Modifiye Karbon Nanotüp Nanokompozitlerinin Karakterizasyonu ve Termal Kinetik Özellikleri*, Doktora Lisans Tezi, Balıkesir Üniversitesi Fen Bilimleri Enstitüsü, Balıkesir-Türkiye.

Bal, A. (2021). *Bursa İli Çaybaşı Bölgesi Maden Suyu Kaynaklarında Organoklorlu Pestisit Kalıntılarının İncelenmesi*, Yüksek Lisans Tezi, Bursa Teknik Üniversitesi Fen Bilimleri Enstitüsü, Bursa-Türkiye.

Baykal, A., Günay, M., Toprak, M.S. and Sozeri, H. (2013). Effect of ionic liquids on the electrical and magnetic performance of polyaniline–nickel ferrite nanocomposite. *Mater. Res. Bull*., 48, 378.

Bayrak, A. (2012). *Manyetik Nano Parçacıkların (MNP) Kontrollü Sentezi ve Yüzey Modifikasyonu ile Polimerleşme Tepkimelerinde Kullanımları*, Yüksek Lisans Tezi, İnönü Üniversitesi Fen Bilimleri Enstitüsü, Malatya-Türkiye.

Bowen G. J. (2010). Isoscapes: spatial pattern in isotopic biogeochemistry. *Annual Review of Earth and Planetary Sciences*, 38, 161-187.

Cerling T.E., Barnette J.E., Bowen G.J., Chesson L.A., Ehleringer J.R., Remien C.H., Patrick S., Tipple B. and West J.B. (2016). Forensic stable isotope biogeochemistry . *Annu. Rev. Earth Planet. Sci*., 44, 175-206.

Cha, J. and Kwon, I. (2018). Purification-free, target-seşective immobilization of a protein from cell lysates. *Biotechnol. J*., 13, 1700739.

Chung, D.D.L. (2000). Materials for electromagnetic interference shielding. *J. Mater. Eng. Perform.* 9, 350-354.

D'Arcy, B.M., Arrington, J., Weisman, J., McClellan, S.B., Yang, Z., Deivanayagam, C., Blount, J., Prakash, A. (2022). PMS2 variant results in loss of ATPase activity without compromising mismatch repair. *Molecular Genetics & Genomic Medicine*, 10(5), e1908.

Ehleringer, J.R., Bowen, G.J., Chesson, L.A., West, A.G., Podlesak, D.W., Cerling, T.E. (2008). Hydrogen and oxygen isotope ratios in human hair are related to geography. *PNAS*, 105(8): 2788-2793.

Fang, M., Ivanisevic, J., Benton, H.P., Johnson, C.H, Patti, G.J, Hoang, L.T, et al. (2015). Thermal degradation of small molecules: a global metabolomic investigation. *Analytical Chemistry, 87(21),* 10935–10941.

Golezani, J.J., Kartal, M., Döken, B., Paker, S. (2022). Trible-Band frequency selective surface design effective over oblique incidence angles for GSM system. *IETE Journal of Research*, 68(2), 1406-1410.

Göktürk, P. A. (2018). *X-Ray Phptoelectron Spectroscopy For Chemical and Electrical Characterization of Devices Extended to Liquid/Solid Interfaces*, Doktoral Thesis, The Graduate School of Engineering and Science of Bilkent University, Ankara-Turkey.

Gümüş, H. (2010). *Ham ve Ön-İşlem Görmüş Sepiyolit Numunelerinin Cu(II) ve Pb(II) Alıkoyma Davranışlarının XRD, XRF, FTIR, Termik Analiz ( TG-DTA), Atomik Absorpsiyon Teknikleriyle İncelenmesi*, Yüksek Lisans Tezi, Dumlupınar Üniversitesi Fen Bilimleri Enstitüsü, Kütahya-Türkiye.

Harris, Daniel C. (2007). *Quantitative Chemical Analysis*. 7th Edition. W.H. Freeman and Company, New York.

He, F., Si, K., Li, R., Zha, D., Dong, J, Miao, L., Bie, S., Jiang, J. (2022). Frequency selective surface composites with honeycomb absorbing structure for broadband applications. *IEEE Transactions on Antennas and Propagation.* 70(9), 8643-8647.

Helmers, T., Kemper, P., Thöming, J., Mießner, U . (2022). Taylor flows in square microchannels. *Experiments in Fluids. 63*(1), 5.

Ibrahim, J.F.M., Mergen, A., Sahin, E.İ., Basheer, H.S. (2017). The effect of europium doping on the structural and magnetic properties of $GdMnO_3$ multiferroic ceramics. *Advanced Ceramics Progress*, 3(4), 1-5.

Ibrahim, J.E. (2015). *Enhancement of Structural and Magnetic Properties of Eu and Fe Doped $GdMnO_3$ and Cr Doped $HoMnO_3$ Multiferroic Ceramics*, Master Thesis, Marmara University Institute For Graduate Sturdies In Pure and Applied Sciences, İstanbul-Turkey.

Jones, M. (2019). *Gas Chromatography-Mass Spectrometry*. American Chemical Society.

Kartal, M., Pinar, S. K., Döken, B., & Gungor, I. (2013). A new narrow band frequency selective surface geometry design at the unlicensed 2.4-GHz ISM band. *Microwave and Optical Technology Letters*, 55(12). 2986-2990.

Khairy, M. (2014). Synthesis, characterization, magnetic and electrical properties of polyaniline/$NiFe_2O_4$ nanocomposite. *Synthetic Met*., 189, 34.

Khairy, M. and Gouda, M.E. (2015). Electrical and optical properties of nickel ferrite/polyaniline nanocomposite. *J. Adv. Res.*, 6, 555.

Kıvrak, İ. (2013). *Tuber aestivum ve Calvatia gigantea Mantarlarının Kimyasal Bileşimlerinin Headspace GC/MSD, HPLC/DAD-RID ve UPLC-MS/MS Sistemleri ile Analizi, Antioksidan ve Antikolinesteraz Aktivitelerinin Belirlenmesi*, Doktora Tezi, Muğla Sıtkı Koçman Üniversitesi Fen Bilimleri Enstitüsü, Muğla-Türkiye.

Kostogloudis, G. Ch., Fertis, P., Ftikos, Ch. (1998). The perovskite oxide system $Pr_{1-x}Sr_xCo_{1-y}Mn_yO_{3-\delta}$: crystal structure and thermal expansion. *Journal of the European Ceramic Society*, 18(14), 2209-2215.

Lin, T., Yu, H., Wang, L., Fahad, S., Khan, A., Naveed, K.-Ur-R., Haq, F., Nazir, A. and Amin, B. U. (2021). A review of recent advances in the preparation of polyaniline-based composites and their electromagnetic absorption properties. *J. Mater. Sci*., 56, 5449-5478.

Liu, P.B., Huang, Y., Wang, L., Zong, M., Zhang, W. (2013) Hydrothermal synthesis of reduced graphene oxide-$CO_3O_4$ composites and the excellent microwave electromagnetic properties. *Mater Lett*., 107, 166–169.

Liu, Y.J., Hou, Q.Y., Xu, Z.C. *et al.* (2019). Effects of Ag Doping and Point Defect on the Magnetism of ZnO. *Journal of Supercondivity and Novel Magnetism,* 32, 2097–2106.

Luo, J.H., Xu, Y., Yao, W., Jiang, C.F., Xu, J.G. (2015). Synthesis and microwave absorption properties of reduced graphene oxide-magnetic porous nanospheres-polyaniline composites. *Compos. Sci. Technol*., 117, 315–321.

Meisak, D., Plyushch, A., Macutkevič, J., Grigalaitis, R., Sokal, A., Lapko, K.N., Selskis, A., Kuzhir, P.P., Banys, J. (2023). Effect of temperature on shielding efficiency of phosphate-bonded $CoFe_2O_4$–$xBaTiO_3$ multiferroic composite ceramics in microwaves. *Journal of Materials Research and Technology*, 24, 1939-1948.

Mergen, A., Eroğlu, M.S. et al. (2010). *Kimyasal yöntemlerle nano boyutta $Ba(Zn_{1/3}Nb_{2/3})O_3$ ve $MNb_2O_6$ ( M=Zn, Co, Mg) bazlı mikrodalga dilektrik seramiklerin üretimi ve farklı katkıların özelliklere etkileri*, Tübitak Mag Proje, Proje No: 107M372.

Mert, E., Aras, A. (2022). Analysis of Volatile Organic Compounds Considered to Have Harmful Effects on Human Health in Iğdır Central and Some Village Schools. *Journal of the Institute of Science and Technology*, 12(4), 2322 - 2330.

Nedic, O., Sunderic, M., Robajac, D., Miljus, G., Cetic, D., Penezic, A. (2022) Major trace elements and their binding proteins in the early phase of Covid-19 infection. *JBIC Journal of Biological Inorganic Chemistry*, 27, 261-269.

Peng, S., Zhang, Y. and Yi, T. (2022). Research Progress of $Ba(Zn_{1/3}Nb_{2/3})O_3$ microwave dielectric ceramics. *A review. Materials*, 16, 423.

Qasrawi, A.F., Hamarsheh, A.A. (2022). Structural, optical and electrical properties of band-aligned $CdBr_2/Au/Ga_2S_3$ interfaces and their application as band filters suitable for 5G technologies. *J. Electronic Materials*, 32, 1-12.

Qasrawi, A.F., Sahin, E.İ, Emek, M., Kartal, M. and Kargin, S. (2019). Structural and dielectric performance of the $Ba(Zn_{1/3}Nb_{2/3-x}Sb_x)O_3$ perovskite ceramics. *Materials Research Express*, 6, 095095.

Qasrawi, A.F., Sahin, E.İ, and Emek, M. (2021). Nickel doping effects on the structural and dielectric properties of $Ba(Zn_{1/3}Nb_{2/3})O_3$ perovskite ceramics. *Journal of Electronic Materials*, 50(4), 2223-2231.

Qasrawi, A.F., Sahin, E.İ., Abed, T.Y., Emek, M. (2021). Structural and dielectric properties of $Ba_{1-x}La_x(Zn_{1/3}Nb_{2/3})O_3$ solid solutions. *Phys. Status Solidi B*, 258, 2000419-2000436.

Rodrigues C., Brunner M., Steiman S., Bowen G. J., Nogueira J. M. F., Gautz L., Prohaska T. and Máguas C. (2011). Isotopes as tracers of the Hawaiian coffee-producing regions. *Journal of Agricultural and Food Chemistry*, 59, 10239-10246.

Rodoń, A., Łukowiec, D., Kremzer, M., Mikuła, J., Włodarczyk, P. (2018). Electrical conduction mechanism and dielectric properties of spherical shaped $Fe_3O_4$ nanoparticles synthesized by co-precipitation method. *Materials*, 11(5), 735.

Sparkman, D.O., Penton, Z., Kitson, F.G. (2011). *Gas Chromatography and Mass Spectrometry: A Practical Guide*. Academic Press.

Shukla, V. (2020). Role of spin disorder in magnetic and EMI shielding properties of $Fe_3O_4$/C/PPy core/shell composites. *Journal of Material Science*, 55, 2826-2835.

Sun, X., He, J., Li, G., Tang, J., Wang, T., Guo, Y., and Xue, H. (2013). Laminated magnetic graphene with enhanced electromagnetic wave absorption properties. *Journal of Materials Chemistry C*, 1, 765–777.

Şahin, E. İ. & Emek, M. (2023). ELEKTROMANYETİK KİRLİLİK ORTAMINDA KAOLİNİT/PVA KOMPOZİTLERİN ELEKTROMANYETİK KALKANLAMA ÖZELLİKLERİ . *İstanbul Ticaret Üniversitesi Fen Bilimleri Dergisi*, 22(43). https://doi.org/10.55071/ticaretfbd.1252709

Şahin, E.I, Emek, M., Ertug, B., Kartal, M. (2020). Electromagnetic shielding effectiveness of Colemanite/PANI/$SiO_2$ composites radar and wider frequency ranges. *Beykent University Journal of Science and Engineering*, 13, 34-42.

Şahin, E.İ. (2022). Microwave electromagnetic shielding effectiveness of $ZnNb_2O_6$-chopped strands composites for radar and wideband (6.5-18 GHz) applications. *Lithuanian Journal of Physics*, 62(3), 161-170.

Şahin, E.İ., Emek, M., Ibrahim, J.E.F.M. (2022). CuO/PANI/Kolemanit kompozitlerin geniş bant elektromanyetik ekranlama etkinliği. E. Orhan ve E. Seven (Yay. haz.). *TEORİDEN UYGULAMAYA FİZİK VE MATEMATİK ALANINDA AKADEMİK ÇALIŞMALAR (s. 121-137).* Ankara: İksad Publishing House.

Şahin, E.İ. & Cantürk, S.B. (2023). Corrosion properties of CuSnSi alloy in different mediums. S. Güldal (Yay. haz.). *SYSTEMATIC INVESTIGATIONS FOR INDUSTRIAL DEVELOPMENT (*s. 81-101*).* Ankara: İksad Publishing House.

Şahin, E.İ., Emek, M., Ibrahim, Jamal-Eldin F.M. (2023). İletişim uygulamaları için mikrodalga dilektrik $Ba(Zn_{1/3}Nb_{2/3})O_3$ malzemelerin incelenmesi. S. Güldal (Yay. haz.). *FEN VE MÜHENDİSLİKTE ANALİZ, SENTEZ VE UYGULAMALAR (*s. 67-81*).* Ankara: İksad Publishing House.

Şahin, E.İ. (2023). 0-8 GHz uygulamalar için Kaolinit/PANI/Kolemanit kompozitlerin elektromanyetik ekranlama ölçümleri. M. F. Baran (Yay. haz.). *BİYOSİSTEM MÜHENDİSLİĞİ AKADEMİK ÇALIŞMALARI I (s. 249-265). Ankara:* İksad Publishing House.

Şahin, E.İ. (2023). Electromagnetic shielding effectiveness of $Ba(Zn_{1/3}Nb_{2/3})O_3$:Chopped strands composites for wide frequency

applications. *Journal of Ceramic Processing Research*, 24(1), 190-196.

Şahin, E.İ., Emek, M., Ibrahim, J.E.F.M. *et al.* (2023). Shielding effectiveness performance of polyaniline-$NiFe_2O_4$:Cu composites for sub-8 GHz applications. *Optical and Quantum Electronics,* 55, 500.

Şahin, E.İ., Canturk, S.B., Emek, M., Genç, S., Kartal, M. (2021). Production and microwave electromagnetic shielding effectiveness of polyaniline-$La_2Ti_2O_7$:Er,Yb composites. *Journal of Ceramic Processing Research*, 22(2), 208-213.

Şahin, E.İ. (2019). *Katkılı $NiFe_2O_4$ Polimer Tabanlı Mikrodalga Yutucuların Frekans Seçici Malzeme Tasarımı*, Doktora Tezi, İstanbul Teknik Üniversitesi Bilişim Enstitüsü, İstanbul-Türkiye.

Şahin, E.İ. (2010). *Yeni $Ba(Zn_{1/3}Nb_{2/3})O_3$ Bazlı Dielektrik Malzemelerin Üretimi ve Karakterizasyonu*, Yüksek Lisans Tezi, Marmara Üniversitesi Fen Bilimleri Enstitüsü, İstanbul-Türkiye.

Şahin, E.İ., Emek, M., Kartal, M., Pınar, S. K., Kargin, S., Cantürk, S.B. (2020, January). *Production and magnetic properties Mo:$NiFe_2O_4$ composites.* EJONS IX- INTERNATIONAL CONFERENCE ON MATHEMATICS-ENGINEERING-NATURAL & MEDICAL SCIENCES, Marrakech Morocco.

Ting, T.H., Yu, R.P., Jau, Y.N. (2011). Synthesis and microwave absorption characteristics of polyaniline/NiZn ferrite composites in 2–40 GHz. *Mater. Chem. Phys*., 126, 364-368.

Topcu, İ. (2021). Mechanical properties of PLA and ABS parts produced with fused filament fabrication method. *Journal of Ceramic Processing Research*. 22(2), 143–148.

Topcu, İ., Ceylan, M., Yılmaz, E.B. (2020). Experimental investigation on mechanical properties of multi wall carbon nanotubes (MWCNT) reinforced aluminium metal matrix composites. *Journal of Ceramic Process Research*, 21(5), 596-601.

Topcu, İ., Ceylan, M. (2020). Wear behavior of irregular shape Ti6Al4V powder reisforced with carbon nanotubes. *Journal of Ceramic Process Research*, 21(5), 539-546.

Topcu, İ. (2020). Investigation of wear behavior of particle reinforced AL/B4C composites under different sintering conditions. *Tehnicki Glasnik*, 14(1), 7-14.

Topcu, İ. (2022). Sol-Jel yöntemi ile üretilen silica tabanlı hidrofobik aerojellerin karakterizasyon özelliklerinin incelenmesi. *Avrupa Bilim ve Teknoloji Dergisi*, 45, 1-7.

Ucar, N., Kayaoglu, B.K., Bilge, A., Gurel, G., Sencandan, P. And Paker, S. (2018). Electromagnetic shielding effectiveness of carbon fabric/epoxy composite with continuous graphene oxide fiber and multiwalled carbon nanotube. *J. Compos. Mater*., 52(24), 3341-3350.

Uçar, B. (2011). *İyon Kromatografi Kullanarak Çeştili Örneklerde Perklorat Analizi ( Musluk Suyu, Havuz Suyu, Yüzey Suyu, Süt)*, Yüksek Lisans Tezi, İstanbul Teknik Üniversitesi Fen Bilimleri Enstitüsü, İstanbul-Türkiye.

Uniyal, P. and Yadav, K.L. (2009).Room temperature multiferroic properties of Eu doped $BiFeO_3$. *J. Appl. Phys*., 105(7), 07D914.

Wang, L., Long, F., Chen, Y., Xiong, H., Rehman, S. U., Chang, J., Zhong, Z. (2021). Optimization of the microwave absorption properties of FeSiCr@$Fe_2O_3$core-shell nanoparticles by controlling the thickness and crystallinity of $Fe_2O_3$ shell. *Journal of the American Ceramic Society*, 105, 4171-4179.

Yang, S., Lozano, K., Lomeli, A., Foltz, H.D. and Jones, R. (2005). Electromagnetic interference shielding effectiveness of carbon nanofiber/LCP composites. *Composites Part A*, 36(5), 691-697.

Yılmaz, N.S. (2013). *Aydın ve Çevresindeki jeotermal sulardaki bazı elementlerin ve iyonların ICP-OES ve IC ile analizi*. Yüksek Lisans Tezi, Adnan Menderes Üniversitesi Fen Bilimleri Enstitüsü, Aydın-Türkiye.

Zhu, C., Chen, A., Mao, J., Wu, G., Li, S., Dong, X., Li, G., Jiang, Z., Song, Y., Chen, W. and Wei, W. (2023). Cu-Pd biomteallic gas diffusion electrodes for electrochemical reduction of $Co_2$ to $C_{2+}$ products. *Small Structures*, 4, 2200328.


ISBN: 978-625-367-083-2